AD-A132 248 SPATIAL FILTERING FOR ENHANCING POINT TARGETS IN IMAGES FROM A SPACE-BASED MOSAIC IR DETECTOR(U) DEFENCE RESEARCH ESTABLISHMENT VALCARTIER (QUEBEC) J F BOULTER

1/1

UNCLASSIFIED JUL 83 DREV-4287/83 F/G 17/5 NL

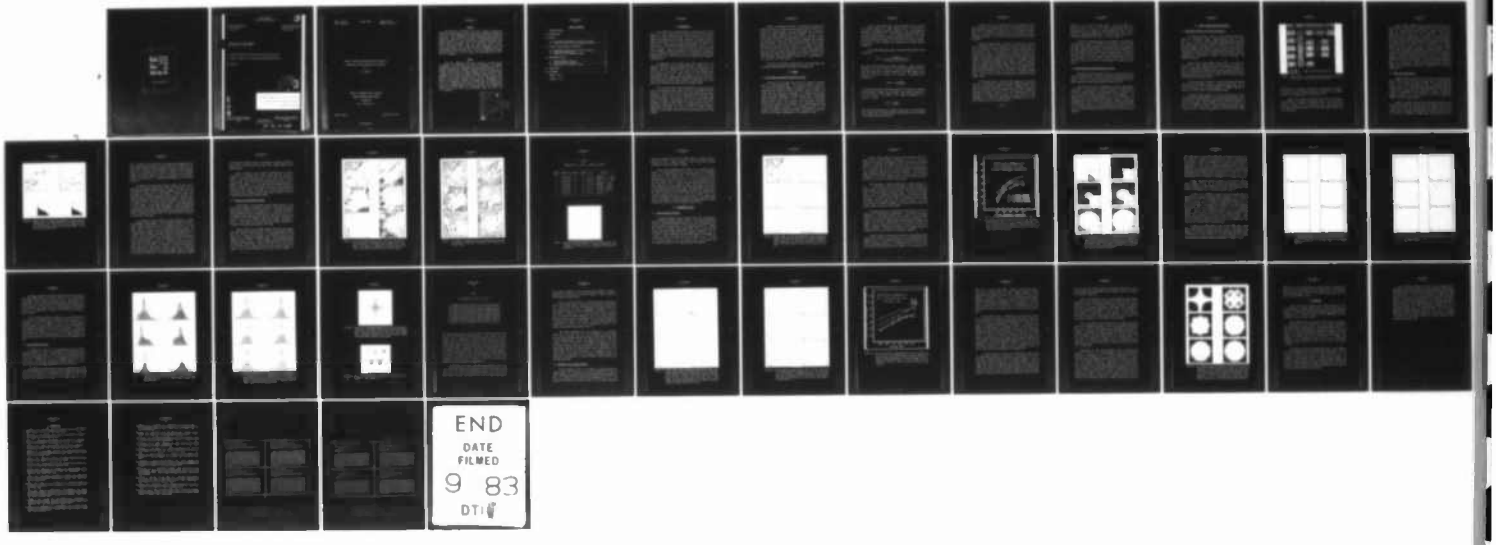

END

DATE FILMED

9 83

DTIC

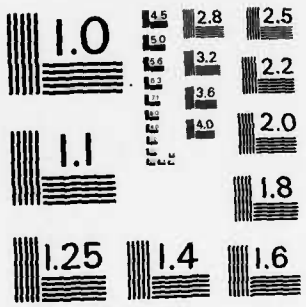

UNCLASSIFIED
UNLIMITED DISTRIBUTION

DREV REPORT 4287/83
FILE: 3633A-016
JULY 1983

CRDV RAPPORT 4287/83
DOSSIER: 3633A-016
JUILLET 1983

SPATIAL FILTERING FOR ENHANCING POINT TARGETS IN IMAGES FROM A SPACE-BASED MOSAIC IR DETECTOR

J.F. Boulter

Centre de Recherches pour la Défense
Defence Research Establishment
Valcartier, Québec

BUREAU - RECHERCHE ET DÉVELOPPEMENT
MINISTÈRE DE LA DÉFENSE NATIONALE
CANADA

NON CLASSIFIÉ
DIFFUSION ILLIMITÉE

RESEARCH AND DEVELOPMENT BRANCH
DEPARTMENT OF NATIONAL DEFENCE
CANADA

DREV R-4287/83 UNCLASSIFIED CRDV R-4287/83
FILE: 3633A-016 DOSSIER: 3633A-016

SPATIAL FILTERING FOR ENHANCING POINT TARGETS IN IMAGES FROM A SPACE-BASED MOSAIC IR DETECTOR

by

J.F. Boulter

CENTRE DE RECHERCHES POUR LA DÉFENSE

DEFENCE RESEARCH ESTABLISHMENT

VALCARTIER

Tel: (418) 844-4271

Québec, Canada July/juillet 1983

ABSTRACT

We examined by simulation the use of spatial filtering for enhancing the visibility of point targets and reducing the background clutter in imagery obtained with a space-based staring mosaic IR detector array. An experimental digital image-processing system was employed to interactively process Landsat II images containing simulated point targets. First, we obtained improved target detection and clutter rejection by using filters that produced considerably more high-frequency enhancement than the conventional Wiener filter. Second, convolution filters with large-area point-spread functions (e.g., those with 11 by 11 elements or those implemented with a 2-dimensional FFT algorithm) were more effective at attenuating the edges of extended regions of clutter (e.g., those corresponding to clouds, bodies of water, etc.) than were those with small areas (e.g., 3 by 3 or 5 by 5 elements).

RESUME

Nous avons examiné par simulation l'aptitude du filtrage spatial à rehausser la visibilité des cibles ponctuelles et à réduire l'arrière-plan dans des images obtenues par un système de surveillance, embarqué sur satellites, employant une mosaïque de détecteurs IR. Un système expérimental de traitement numérique d'images fut employé pour traiter interactivement des images obtenues par le satellite Landsat II auxquelles des cibles ponctuelles simulées étaient ajoutées. Premièrement, les filtres qui accentuent les hautes fréquences sont préférables au filtre standard du type Wiener. Ils sont plus efficaces pour détecter les cibles et éliminer l'arrière-plan. Deuxièmement, les filtres convolutionnels utilisant une fonction avec une grande surface (e.g. 11 x 11 éléments ou ceux obtenus en utilisant une transformation de Fourier bidimensionnelle) sont plus efficaces pour éliminer les contours des grands objets de l'arrière-plan (e.g. les nuages, les lacs, etc.) que les filtres avec une petite surface (e.g. 3 x 3 ou 5 x 5 éléments).

TABLE OF CONTENTS

1.0 INTRODUCTION

When viewed from a satellite bearing a mosaic IR detector array (Refs. 1-5), small targets such as aircraft and missiles are usually imaged onto a single detector element. We consider here the problem of digitally enhancing such point-target images in the presence of background clutter (Refs. 6-13), so they can be detected and tracked automatically by a space-based surveillance system (Refs. 1-3 and 14). We limit ourselves to the use of spatial filtering to enhance a single frame of imagery. Temporal processing of a time sequence of images, as well as multispectral processing, will also be employed in operational systems (Refs. 10, 11 and 13), but we do not consider these enhancement techniques here.

The background clutter against which point targets are to be enhanced usually has less high spatial-frequency content than do the targets. Therefore, high-pass spatial filtering can enhance the targets relative to the clutter, and a variety of such techniques have been proposed (Refs. 10-14). Some are based on a form of Wiener filtering (Refs. 15-16) implemented by approximating the filter by a small area point-spread function (PSF) (usually one measuring 3 by 3 elements) and convolving this directly with the digital image.

First, whereas Wiener filtering maximizes the target-to-clutter ratio in a mean-square error sense, it may not be optimum for clutter rejection. Second, a filter with a small point-spread function cannot efficiently reject clutter that is correlated over relatively large areas of the image. In particular, such a filter cannot effectively attenuate the edges of large objects in a scene, such as those corresponding to clouds, lakes or rivers. We examine these two aspects of point-target enhancement and clutter rejection by digital computer simulation using Landsat satellite images containing artificial point targets.

Chapter 2.0 summarizes the theory of point-target enhancement by spatial filtering, and compares direct spatial-domain convolution filtering with frequency-domain filtering implemented with a two-dimensional fast Fourier transform (2-D FFT) algorithm. In Chap. 3.0, we outline the digital image-processing system that we employed to obtain the simulation results, and describe how we generated the simulated satellite images. Simulation results comparing various forms of high-pass spatial filtering are given in Chap. 4.0. In summary, the results show that more effective clutter rejection and point-target enhancement can be achieved by using filters that (1) produce considerably more enhancement at high spatial frequencies than do Wiener filters and (2) have relatively large point-spread functions (e.g., ones measuring 11 by 11 elements or 2-D FFT filters).

This work was performed at DREV during the period November 1981 to July 1982 under PCN 33A16, Space-Based IR Systems Study.

2.0 THEORY

2.1 Point-Target Enhancement by Spatial Filtering

Suppose we have an image that consists of targets of interest added to a cluttered background. If the spatial-frequency contents of the target and background images are different, we can improve the target-to-clutter ratio by spatial filtering. Forms of Wiener filtering have been proposed as techniques for enhancing point targets against cluttered backgrounds in images obtained with a space-based mosaic IR detector array (Refs. 11-13). A Wiener filter is the linear shift-invariant filter that minimizes the mean-square difference between the intensities of the elements in the restored image and those of the ideal signal of interest. In the present situation, it will optimize the amount of energy in the image corresponding to the targets relative to the amount corresponding to the background clutter.

Assume a target image with a power spectrum $S_t(u,v)$ is added to a clutter image with a power spectrum $S_c(u,v)$. The result is degraded by an imaging system that introduces a blur characterized by its Fourier transform $H(u,v)$. In the present application, $H(u,v)$ may represent blurring caused by target or satellite motion, or by jitter or other instabilities present in the platform or the detector optics. The variables u and v represent the horizontal and vertical spatial frequencies.

In the spatial-frequency domain, the Wiener filter (Refs. 15-16) is given by:

$$Q(u,v) = \frac{H^*(u,v)}{|H(u,v)|^2 + S_c(u,v)/S_t(u,v)}$$

where the asterisk denotes the complex conjugate. Assume we have no blurring, i.e., $H(u,v) = H^*(u,v) = 1$ and that the targets are points. The latter means that the power spectrum of the target image is uniform, i.e., $S_t(u,v) = k$ where k is a constant. The Wiener filter simplifies to:

$$Q(u,v) = \frac{k}{k + S_c(u,v)}$$

If we further assume that the point targets are low enough in intensity and few enough in number that they make a very small contribution to the total power in the image at all spatial frequencies, i.e., $S_c(u,v) >> k$, then

$$Q(u,v) = \frac{k}{S_c(u,v)}$$

The filter that optimizes the target-to-clutter ratio of low-intensity point targets has a frequency response proportional to the reciprocal of the power spectrum of the image.

The Wiener filter is an adaptive one that is determined by the power spectrum of the input image. After its application, the power spectrum of the image will be uniform, i.e., it will have been whitened. If a filter whitens the power spectrum of an image, it can be considered equivalent to the Wiener filter required for point-target enhancement.

Wiener filtering optimizes the target-to-clutter ratio, but this is not necessarily the best criterion to use in the present application. In particular, it may be preferable to obtain more rejection of low-frequency clutter at the expense of an overall decrease in the target-to-clutter ratio. The low-frequency clutter may be difficult to remove by other forms of processing, and it could significantly hinder automatic detection and tracking of the targets. For example, inaccuracies in registering successive image frames obtained at different times may prevent frame subtraction (Refs. 17-18) from cancelling the edges of extended areas of clutter. Retention of such edges can present particular difficulties for certain types of tracking algorithms (Refs. 19-20), and as a result the edges may be classified as false target tracks.

In selecting filters to enhance high frequencies or attenuate low ones, it is important to ensure that the frequency response of the filter is as smooth and gradual as possible. High-pass filters with sharp low-frequency cutoffs can introduce artifacts, such as ringing at the edges of objects or regions. One type of high-pass filter that satisfies this smooth-cutoff criterion and which permits an easy adjustment of the amount of high-frequency enhancement is the circularly symmetric class of filters defined by:

$$F(\omega) = \omega^n$$

where $\omega^2 = u^2 + v^2$ and n is a real number. For certain values of n (typically between 2 and 3) these filters approximately whiten the power spectra of the Landsat II images described in Chap. 3.0 and, therefore, represent approximations to the point-target Wiener filter. We examine experimentally this class of filters in Chap. 4.0.

A variety of processing stages will be employed in a space-based IR surveillance system. In addition to the spatial filtering considered here, they include temporal processing, multispectral processing, and target detection and tracking. The optimum spatial filtering cannot be determined without also including the other forms of processing. However, we will show in Chap. 4.0 that in optimizing the overall system performance, one should consider spatial filters which are quite different from the Wiener filter that maximizes the target-to-clutter ratio.

2.2 Frequency-Domain and Spatial-Domain Filtering

The spatial filters described in Sect. 2.1 were defined in the spatial-frequency domain. They can be implemented exactly by calculating the 2-D FFT of an image, multiplying by the specified filter frequency response, and then calculating the inverse 2-D FFT.

Such filters can also be implemented by direct spatial-domain convolution. In this case, the filter is defined by its PSF, which is the result obtained when the frequency-domain filter is applied to an image containing a single point against a zero background. The resulting PSF of the frequency-domain filter is then truncated to a convenient size and convolved with the image. However, as we examine experimentally in Sect. 4.3, the truncation of the filter PSF results in a frequency response that only approximates the desired one, and this can introduce undesired artifacts or deteriorate the filter performance.

3.0 DIGITAL IMAGE-PROCESSING SIMULATION

3.1 Experimental System and Processing Techniques

The results described in Chap. 4.0 were obtained by simulation using the experimental digital image-processing system at DREV (Ref. 21). A variety of general-purpose image-processing algorithms are available, and these are controlled interactively by an operator who gives commands on keyboards or with a track ball. The main processing operations used to obtain the present results include those for performing 2-D FFT filtering, 2-D spatial-domain convolution, intensity transformation, power-spectrum analysis, display enhancement and graphics generation.

Figure 1 shows a block diagram of the system. It is based on a multi-user PDP 11/70 computer, with standard peripherals, which controls two high-speed processing elements. One of the processing elements is a Floating Point Systems Inc. AP120B programmable array transform processor, and the other one is a Comtal Vision One/20 interactive image-processing and display system.

The array processor operates at 12 million operations per second (38-bit words) and permits a variety of processing algorithms, such as 2-D FFT filtering, to be readily programmed in FORTRAN language and applied in several seconds to 256x256-element images.

The Comtal system operates at 141 million operations per second (8-bit words) and permits images to be digitized and processed at real-time TV rates. Live TV video is digitized with a spatial resolution of 512 by 512 elements, and an intensity resolution of 256 levels, at a rate of 30 frames per second. Internal pipeline processors permit convolution (i.e., spatial filtering with a 3x3-element PSF), image

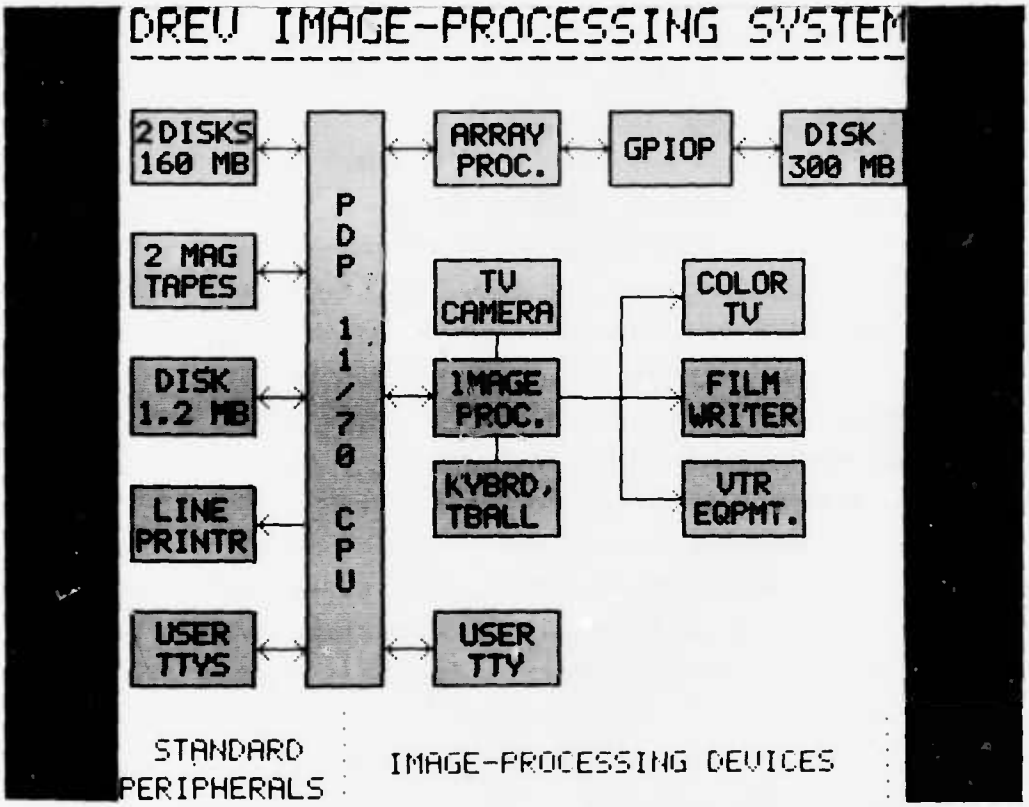

FIGURE 1 - Block diagram of the experimental digital image-processing system used to investigate the spatial filters

combination (i.e., addition, subtraction, multiplication or division of two stored or live TV images), intensity transformation, and pseudo-coloring to be implemented at the real-time TV rate.

Images can be rapidly transferred between the array processor, Comtal system, disk memory and magnetic tape. They can also be recorded on 35-mm, 4- by 5-in Polaroid and 8- by 10-in Polaroid films with a Matrix Instruments model 4007 color graphic camera interfaced to the Comtal system.

The six original Landsat satellite images employed in Chap. 4.0 were recorded on 70-mm positive transparency film. We placed each film image on a light table and viewed it with a high-resolution vidicon camera made by Spatial Data Inc. Four TV frames were digitized, averaged and stored in an image memory. The camera lens was covered and a 16-frame average was similarly acquired and stored. We then subtracted the latter 'black level' digital image from the digitized film image, and minified this by a factor of two by replacing 2- by 2-element squares by their averages to produce a 256- by 256-element image. Point targets were added to this image as described in Sect. 3.2, and the result was processed with 38-bit accuracy in the array processor by using the filtering techniques described in Chap. 4.0. The processed images were normalized, displayed on the Comtal system, and recorded on Polaroid film with the Matrix camera. Most of the figures included in Chap. 4.0 were obtained by using a multiple-image format in which six images were automatically recorded on a single sheet of 8- by 10-in Polaroid film.

3.2 Simulation Approximations

Imagery obtained in the far IR (8-13 μm) with a satellite-based mosaic detector which shows point targets against a cluttered background is not currently available at DREV. We generated simulated images to permit us to investigate the processing techniques that may be employed by a space-based IR surveillance system. The background clutter is represented in the simulation by Landsat II satellite imagery obtained in the near IR (0.8-1.1 μm), and we added point targets to selected image elements.

Objects or regions in a scene will not necessarily have the same relative intensities when viewed with near- and far-IR radiation. This is evident in Figs. 2(A) and 2(B) which give images of the city of Guelph, Ontario, obtained simultaneously in visible light and in the far IR with a multispectral scanner (MSS) located on board an air-

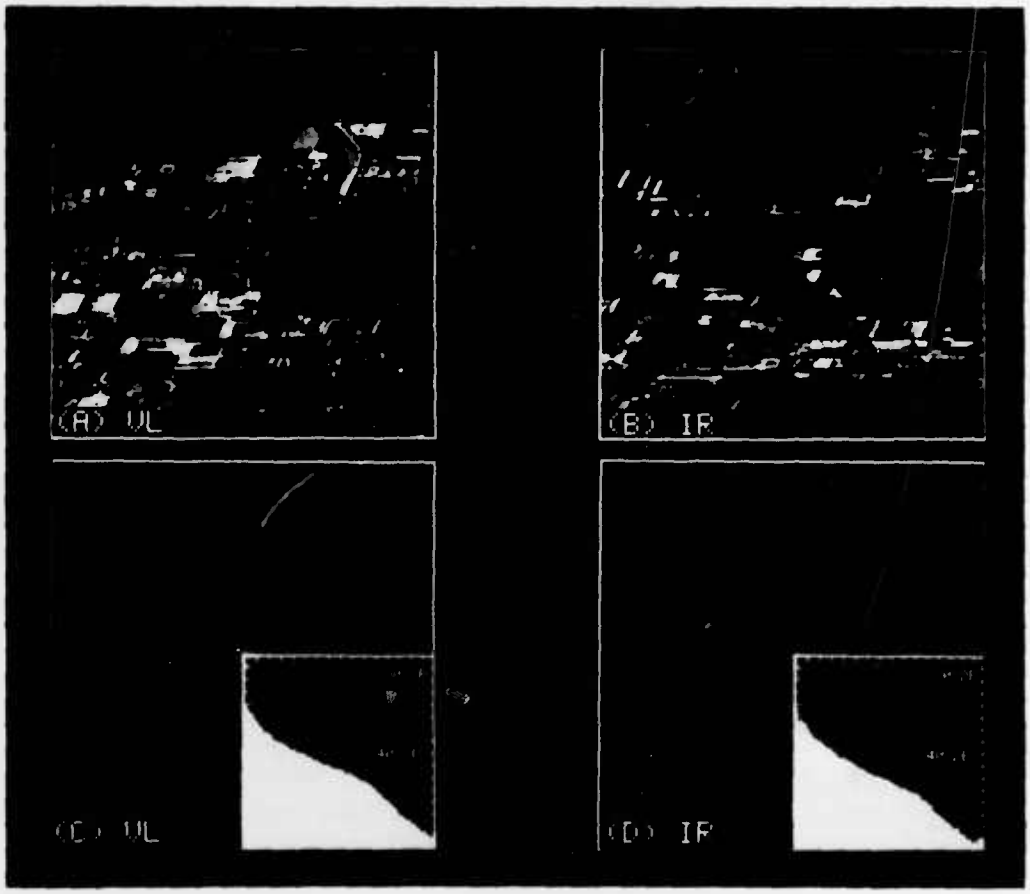

FIGURE 2 - Images from an airborne multispectral scanner obtained simultaneously with visible-light (A) and IR radiation (B). The power spectra (C) and (D) of the two images are similar. The inserts in the power spectra show graphs of their radial power distributions.

craft. However, the visible and far-IR images have approximately the same spatial-frequency content as their power spectra (Figs. 2(C) and 2(D)) show. Since the present processing is based on spatial-frequency content, not directly on the relative contrast of the different regions, the near-IR images that we use to represent the far-IR background clutter should be a reasonable approximation for the present purposes.

We obtained the power spectra shown in Figs. 2(C) and 2(D) by calculating the modulus squared of the 2-D FFT of each image. In each power-spectrum image, the zero spatial frequency is at the center and the Nyquist frequencies are at the borders. The power spectra were displayed with a 4-decade logarithmic intensity scale, therefore full black corresponds to a level 80 dB below the maximum. Since the original images are real, the lower and upper halves of the power spectra are mirror images. In the lower right quadrant of each power spectrum we have graphed its radial power distribution. This was obtained by integrating the power within fixed-thickness rings centered about zero spatial frequency, and plotting this as a linear function of the radius of the center of the ring.

We simulated the point targets by adding constants to a number of nonadjacent image elements. This represents targets that have a higher apparent temperature than the background and which are much smaller than the field of view of an individual detector element. The target images are assumed to be small enough that they always appear on a single detector element, and never overlap two neighboring ones. In practice, the point targets will be broadened by the finite resolution of the imaging system. As will be described in Sect. 3.3, we use images that have been digitized with a relatively low spatial resolution (200 m on the ground). In practice, it should be possible to employ optics with a much higher resolution than this, so there would be no significant broadening of the point targets. However, depending on the size of the gaps (i.e., the inactive areas) between the elements

of the mosaic IR detector array at this spatial resolution, large targets (such as aircraft) may occupy more than a single element in the digital image.

Mosaic IR detector arrays exhibit nonuniformities in overall sensitivity to radiation and in dark current from one element to another. Processing techniques (Refs. 22-23) can be used to reduce these effects. Such point-to-point nonuniformities do not occur in Landsat II MSS images. It is not known how such nonuniformities will affect the ability of high-pass spatial filtering to reduce clutter and enhance the point targets. Approximation of a mosaic detector array by the Landsat MSS is probably the most questionable assumption involved in generating the present simulated images.

3.3 Production of the Simulated Images

We used images of six different scenes acquired in Band 7 of the MSS located on board the Landsat II satellite. The images were formed with near-IR radiation in the range 0.8-1.1 μm, and were recorded on 70-mm black/white positive transparency film. We selected 1.5- by 1.5-cm regions of each film image and digitized these with a spatial resolution of 256 by 256 elements using the procedure described in Sect. 3.1. Each element in the resulting digital images corresponds to a square on the ground measuring 200 m on a side.

Figure 3 shows the six digital images after the point targets have been added as described below. We used homomorphic filtering (Ref. 24) to improve the visibility of low-contrast details in the display and to compress the dynamic range. The resulting enhanced images are given in Fig. 4. The six images represent different types of high-clutter backgrounds. Images A and B show an area in the vicinity of Quebec City in summer, with and without cloud cover, whereas Images C and D show the Montreal area in winter and in summer. A

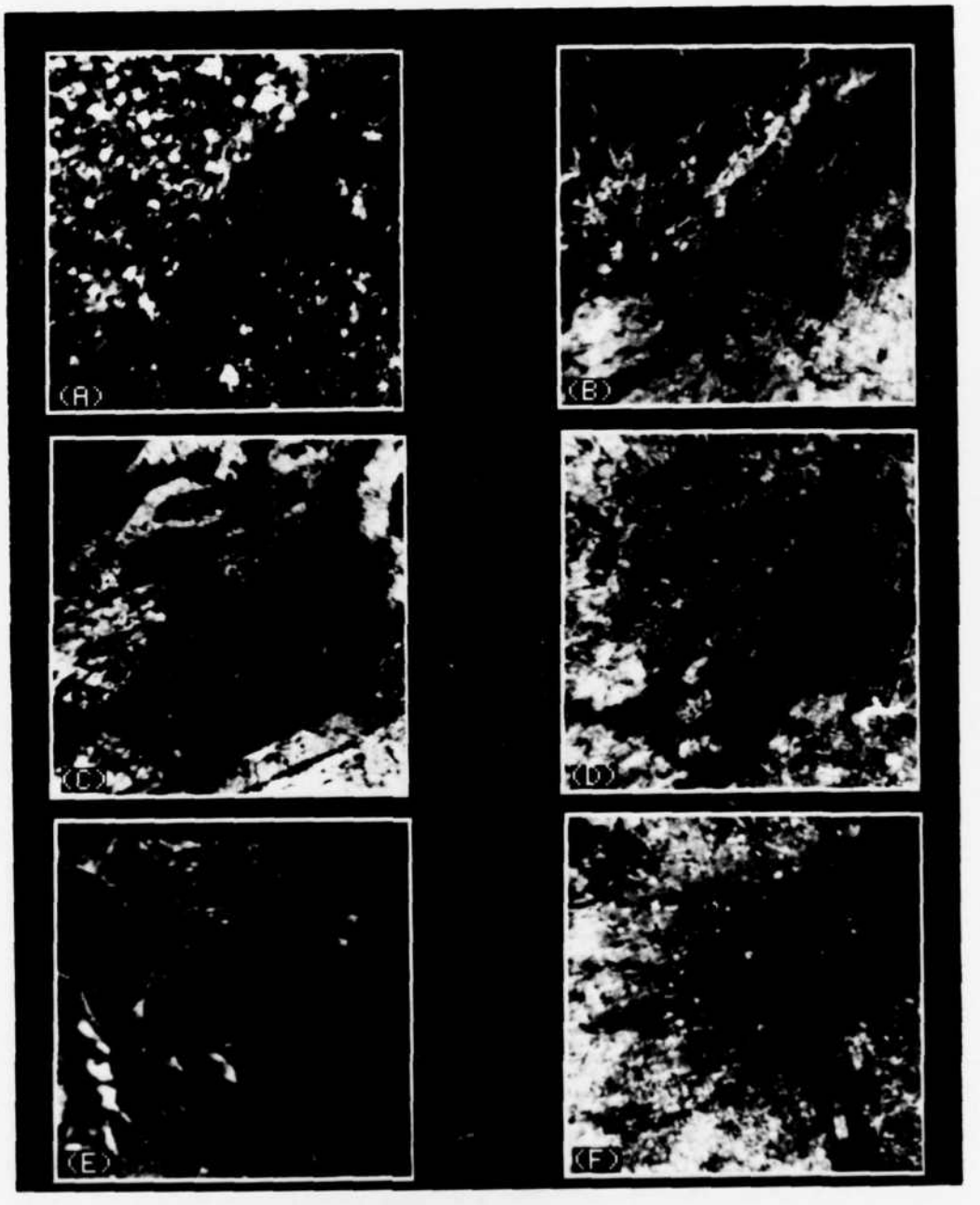

FIGURE 3 - Six near-IR images obtained with the Landsat II satellite. Each represents a different type of high-clutter background, and contains 64 simulated low-intensity point targets. The images are composed of arrays of 256 by 256 elements and have a ground resolution of 200 m/element.

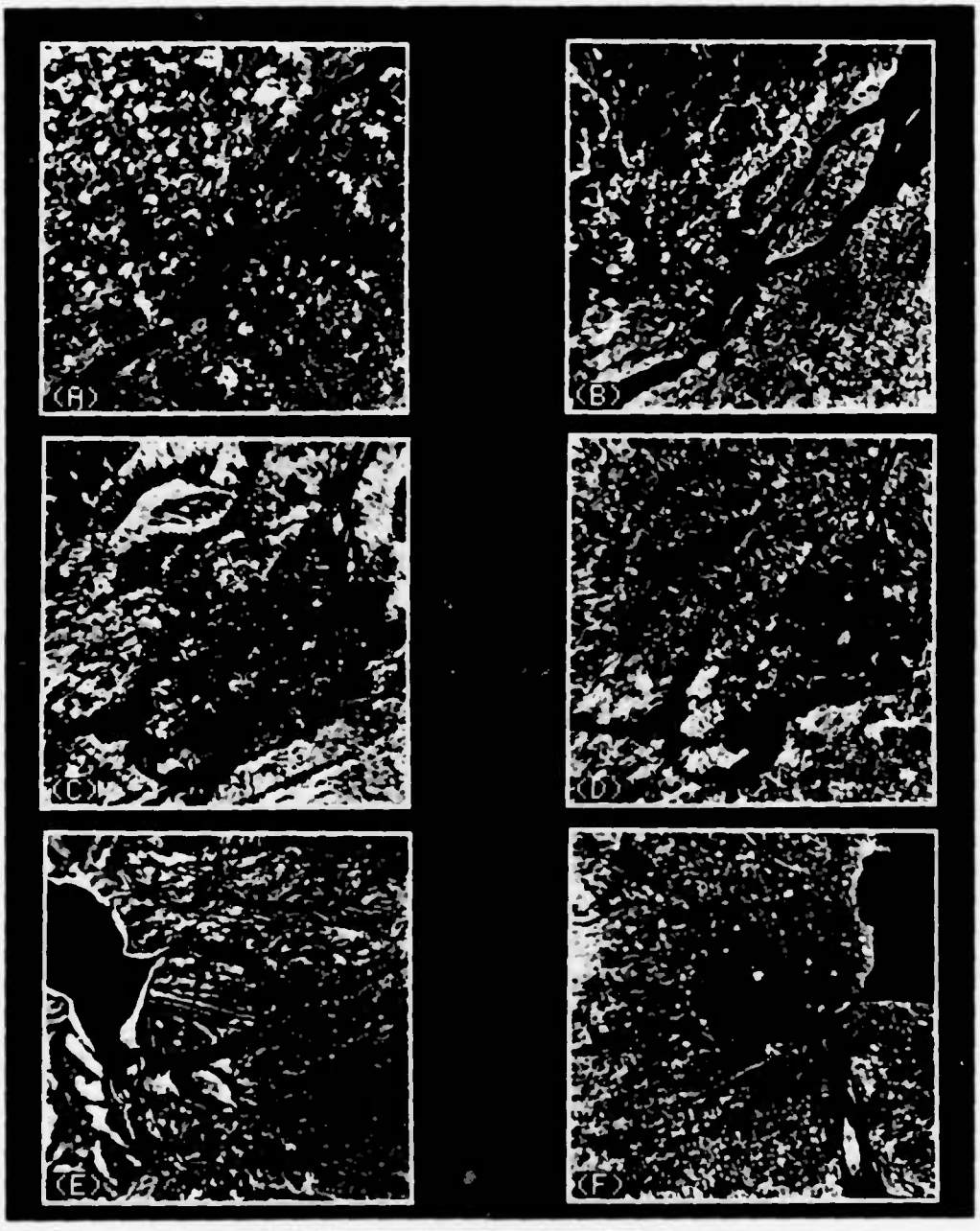

FIGURE 4 - The Landsat II images of Fig. 3 after homomorphic filtering to enhance low-contrast information and compress the dynamic range

TABLE 1

CHARACTERISTICS OF THE SIX LANDSAT II IMAGES

IMAGE	LANDSAT NO	ORBIT	FRAME	DATE	SUBJECT
A	2237814495	14	27	27-07-81	QUEBEC CITY - CLOUDY
B	2239614494	14	27	14-08-81	QUEBEC CITY - CLEAR
C	2212815045	16	28	19-11-80	MONTREAL - WINTER
D	2236215021	16	28	11-07-81	MONTREAL - SUMMER
E	2236715290	21	24	16-07-81	EASTMAN, JAMES BAY
F	2234915320	21	30	28-06-81	DETROIT CITY

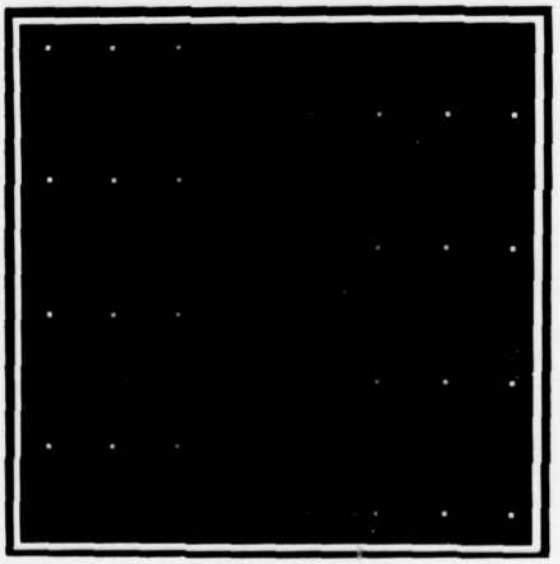

FIGURE 5 - The simulated point targets that were added to each of the Landsat II images of Fig. 3. The point targets have been enlarged to an area of 3 by 3 elements to improve their visibility.

region near James Bay viewed in the summer is given in Image E, and the Detroit City area is shown in Image F. Table I gives more detailed information on the six Landsat II images.

Each of the six images shown in Figs. 3 and 4 contains 64 point targets. As illustrated in Fig. 5, the point targets are arranged in eight rows of eight targets each. The intensities of the targets increase from left to right in rows 1, 3, 5, etc. (counting the rows from the bottom), whereas in rows 2, 4, 6, etc. they increase in intensity from right to left. In each row, the target intensity varies in seven linear steps from a minimum of 0.024M to a maximum of 0.2M, where M is the maximum intensity in the image. The RMS contrast of the average image is 0.146M, so we have generated targets with signal-to-clutter ratios between 0.164 and 1.37. Note that in Figs. 3 and 4 even the most intense point targets are almost invisible in the high-clutter areas of the images, and are only marginally visible against the bodies of water that have more uniform intensity distributions.

4.0 ENHANCEMENT RESULTS

4.1 Frequency-Domain Filtering

We selected Landsat Image A, shown in Fig. 3(A), and applied to it six different high-pass spatial filters. The filters were implemented in the spatial-frequency domain with a 2-D FFT algorithm, and had the power-law response $F(w) = \omega^n$ described in Sect. 2.1. Figure 6(A) shows the original image whereas Figs. 6(B) to 6(F) give the results obtained by using filters with frequency responses ω^2, ω^3, ω^4, ω^6 and ω^8. Before displaying each processed image, we normalized its contrast by setting the black level of the display to $I_A - 1.5\sigma$ and its full-white level to $I_A + 6\sigma$, where I_A and σ are the mean and the standard deviations of the image intensity distribution.

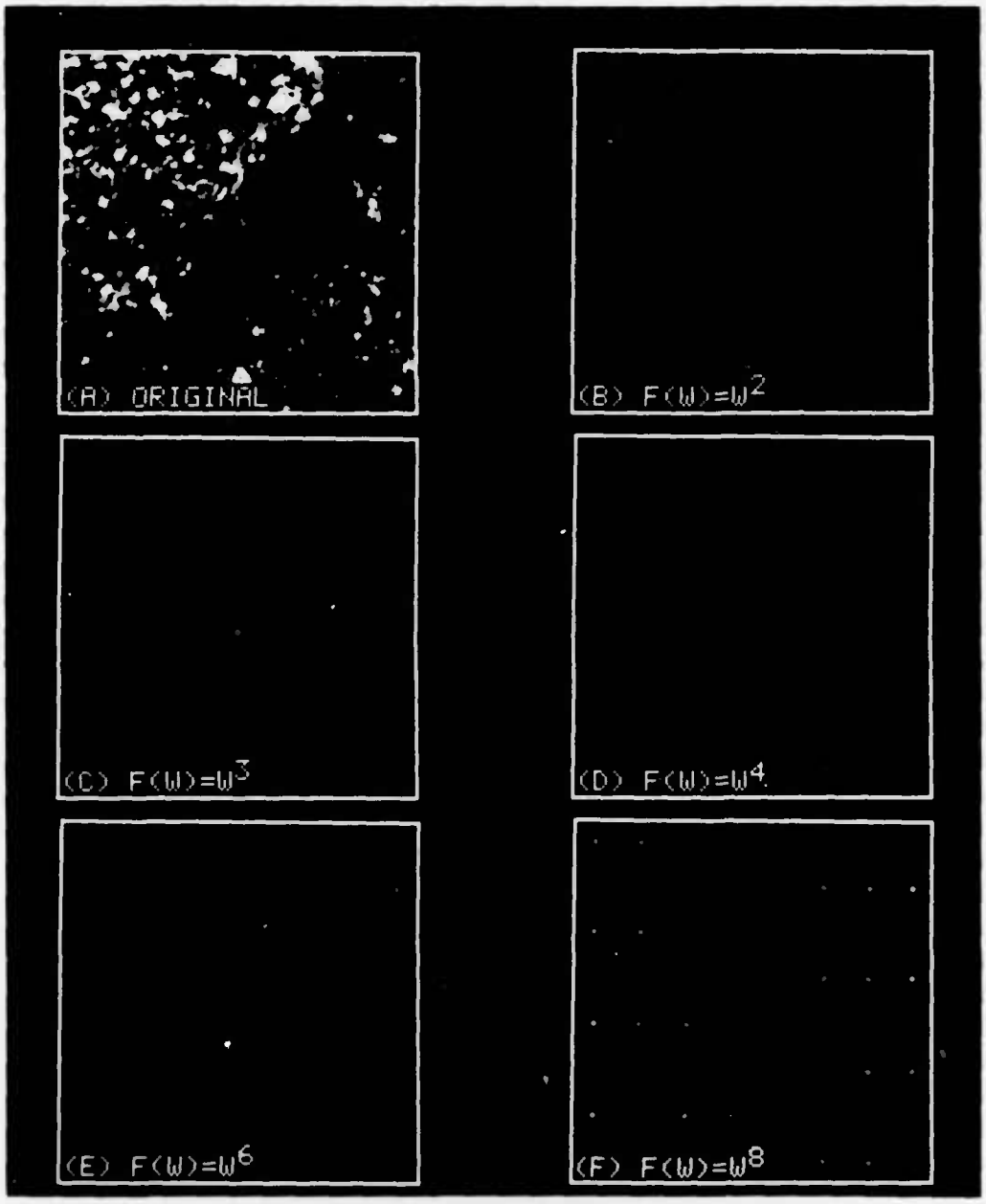

FIGURE 6 - Landsat Image A after five different types of high-pass spatial filtering implemented in the spatial-frequency domain with a 2-D FFT. Increasing the amount of high-frequency enhancement improves the visibility of the point targets and gives better rejection of the background clutter.

Figure 6 clearly shows that filters which produce a small or a moderate amount of high-frequency enhancement (e.g., ω^2 or ω^3) are less effective at reducing the background clutter and enhancing the point targets than are those that produce a larger amount of it (e.g., ω^6 or ω^8). For example, the ω^2 and ω^3 filters retain clutter corresponding to the edges of clouds and the land-water boundaries. These edges are almost completely removed by the ω^6 and ω^8 filters. Note the strong enhancement of the point targets relative to the remaining background clutter that the latter two filters have achieved.

The improvement in target detectability is shown graphically in Fig. 7. In this figure, we plotted the number of targets detected in Landsat Image A as a function of the frequency response of the high-pass filter for four different false-alarm rates. We obtained the upper curve in Fig. 7 by applying a threshold level to each filtered image, adjusting it to obtain 16 false alarms in the image, and then counting the number of point targets that were correctly detected. The lower three curves were similarly obtained by using detection thresholds that produced eight, four and two false alarms.

Increasing the amount of high-frequency enhancement from ω^2 to ω^6 improves the target-detection probability. Note that the detection probability is a nonlinear function of the number of detected targets since the ones present in Landsat Image A have varying intensities. For example, for the curve representing two false alarms, increasing the number of detected targets from 35 (for the ω^2 filter) to 45 (for the ω^6 filter) represents a substantial reduction in the minimum intensity a target must have to be detected with reasonable probability.

Figure 8 gives the power spectra and the corresponding radial distribution functions of the original and the five high-pass filtered images of Fig. 6. We obtained the spectra and the distribution functions as described in Sect. 3.2. As discussed in Sect. 2.1, the filter that whitens the power spectrum of an image, i.e., that modifies it to

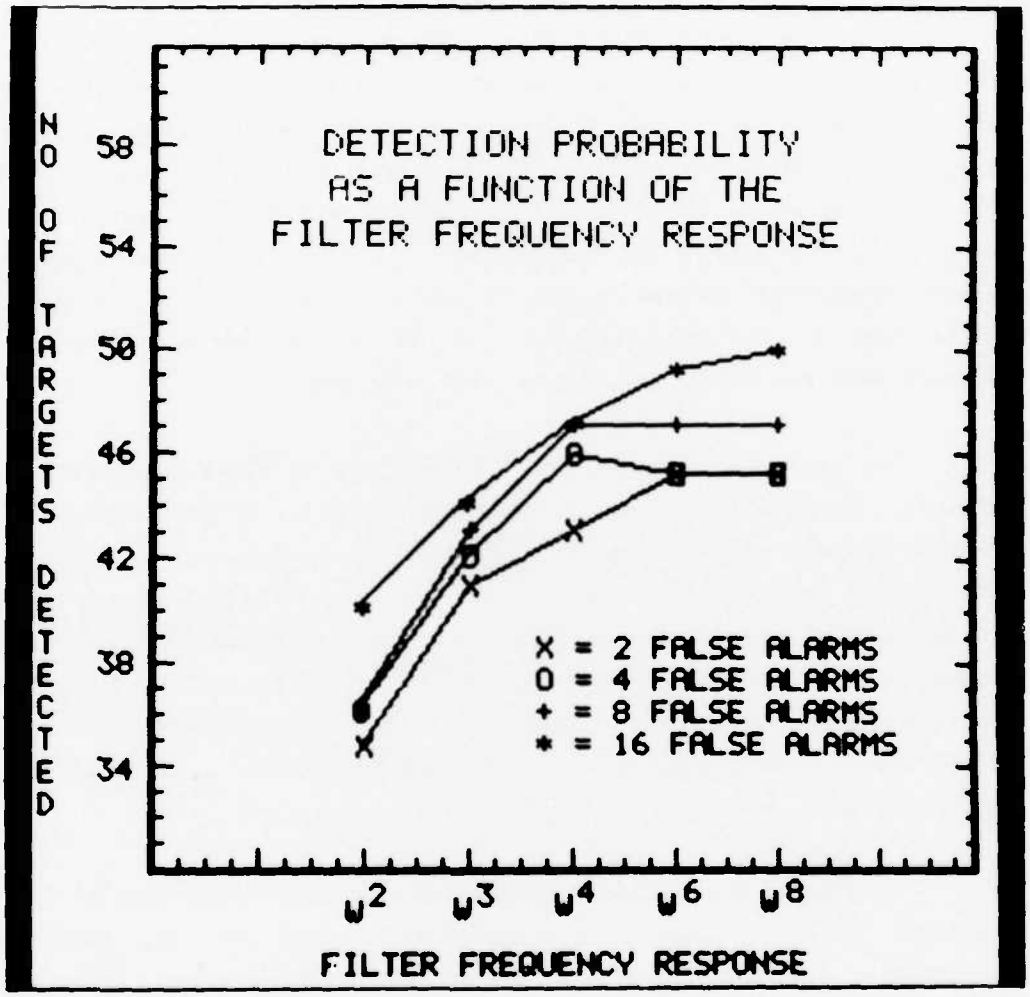

FIGURE 7 - The target-detection performances of the five frequency-domain filters shown in Fig. 6. We generated each of the four curves by setting a single-intensity threshold on the filtered images so as to obtain the specified number of false alarms, and then counting how many of the 64 true point targets were detected.

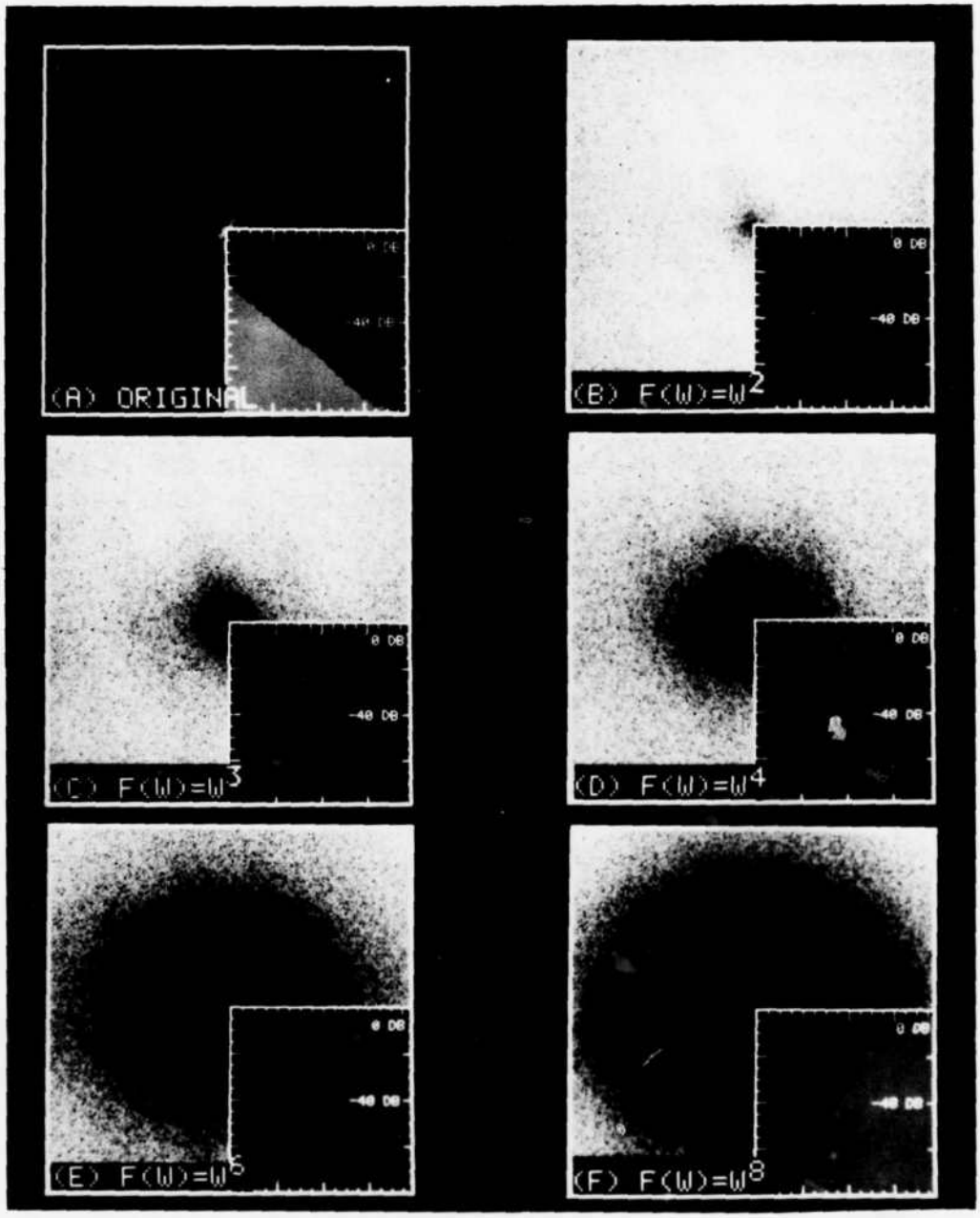

FIGURE 8 - The power spectrum of the original Landsat Image A (A) is shown in (B) to (F) after the application of five different frequency-domain high-pass filters. The inserts in the power spectra show graphs of their radial power distributions. The power spectrum of this image is approximately 'whitened' by a filter with a response proportional to the square or the cube of the spatial frequency.

have equal power at all spatial frequencies, represents the Wiener filter required to optimize the signal-to-noise ratio of low-intensity point targets. Figure 8 illustrates that, except at very low spatial frequencies, a filter with a frequency response between ω^2 and ω^3 approximates the point-target Wiener filter for Image A. Since a much improved target enhancement and clutter rejection is obtained by using considerably more high-frequency enhancement (e.g., $F(\omega) = \omega^6$), the Wiener filter does not appear to be optimum for the present situation.

Figure 9 shows the results of applying the ω^6 filter to the six Landsat images of Fig. 3. In all cases the high-pass filtering strongly enhanced the point targets and suppressed the background. The display normalization was the same as that used in Fig. 6.

In Fig. 10, we attempted to extract the point targets from the background by setting a single-intensity threshold on the filtered images of Fig. 9. If an element had an intensity below $I_A + 6\sigma$ it was set to black, and if it equaled or exceeded this threshold it was set to full white. To improve the visibility of the point targets extracted in Fig. 10, we enlarged each target to a 3- by 3-element square. Only 11 false alarms are present in the six thresholded images, and 266 out of the 384 points were correctly detected. All targets with an intensity of 0.656σ or higher were detected. Those with an intensity of 0.492σ were detected with a 50% probability, but only 2% of the 0.328σ targets were extracted.

Increasing the high-frequency content of the background clutter made it more difficult to detect the point targets. For example, the targets that were present against the lower frequency backgrounds shown in Images B and E were detected with a higher probability than those present against the higher frequency backgrounds of Images A and F.

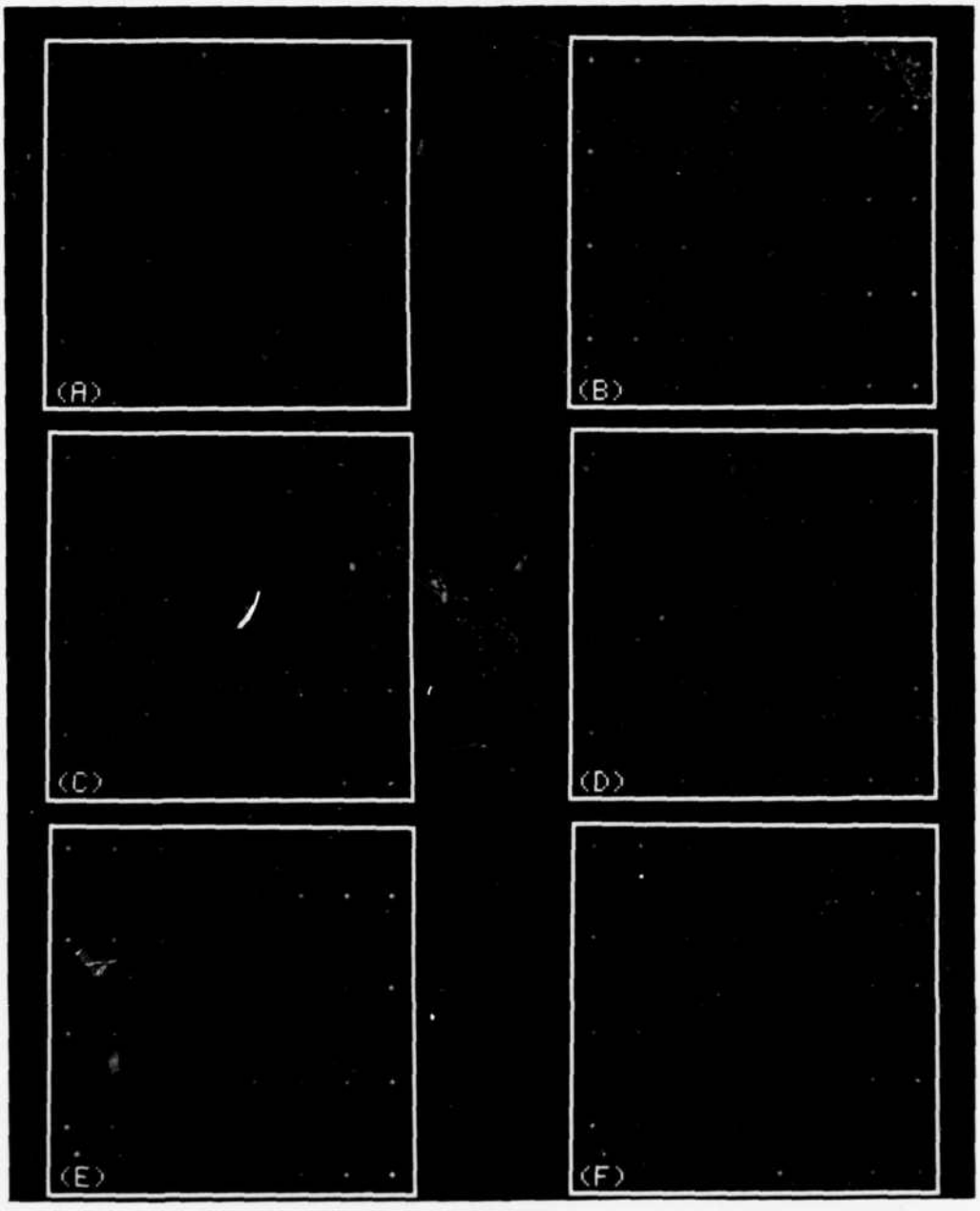

FIGURE 9 - The six Landsat images of Fig. 3 after high-pass filtering to enhance the point targets and reduce the background clutter. The filter was the same for all cases and had a response proportional to the sixth power of the spatial frequency.

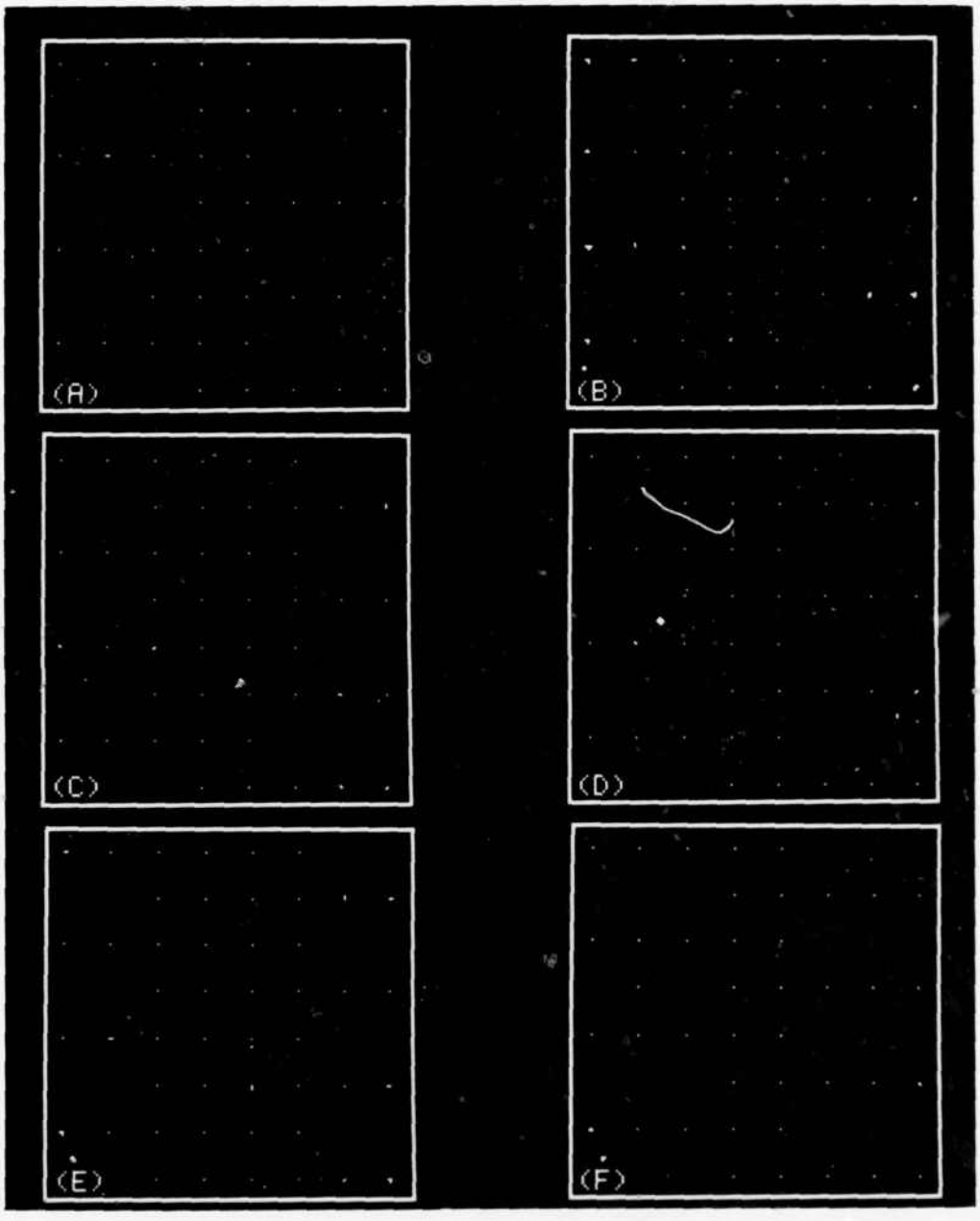

FIGURE 10 - The six high-pass filtered Landsat images of Fig. 9 after setting a single-intensity threshold at $I_A + 6\sigma$ to detect the point targets

Histograms showing the intensity distributions of the six original Landsat images of Fig. 3 are given in Fig. 11. Most distributions are bimodal, with the sharp low-intensity peak corresponding to the darker water areas and the broader mid-intensity peak corresponding to the land areas. As shown in Fig. 12, after high-pass filtering with $F(\omega) = \omega^6$, all images have an intensity distribution that is approximately Gaussian.

This is opportune because it permits us to use normal statistics in analyzing and implementing the target-extraction operation. In particular, to detect the targets in each of the present high-pass filtered images, it was necessary to calculate only two parameters of the intensity distribution: its mean and its variance. By setting a fixed-intensity threshold at $I_A + 6\sigma$, we obtained an acceptable balance between miss and false-alarm rates for all images, despite the significant differences in the characteristics of the background clutter.

4.2 Spatial-Domain Filtering

As described in Sect. 2.2, the implementation in the spatial-frequency domain of a filter is equivalent to the convolution of its PSF with the original image. In this section we calculate the PSF of the ω^6 filter employed in Sect. 4.1, and examine the effect of truncating it. In particular, we apply to Landsat Image A 3x3-, 5x5-, 7x7-, 9x9- and 11x11-element approximations of the ω^6 filter.

We generated the PSF of the ω^6 filter by calculating the 2-D FFT of an image containing a point against a zero background, multiplying this by the function ω^6 and performing the inverse 2-D FFT. The resulting PSF, enlarged by a factor of 4, is shown in Fig. 13. Only

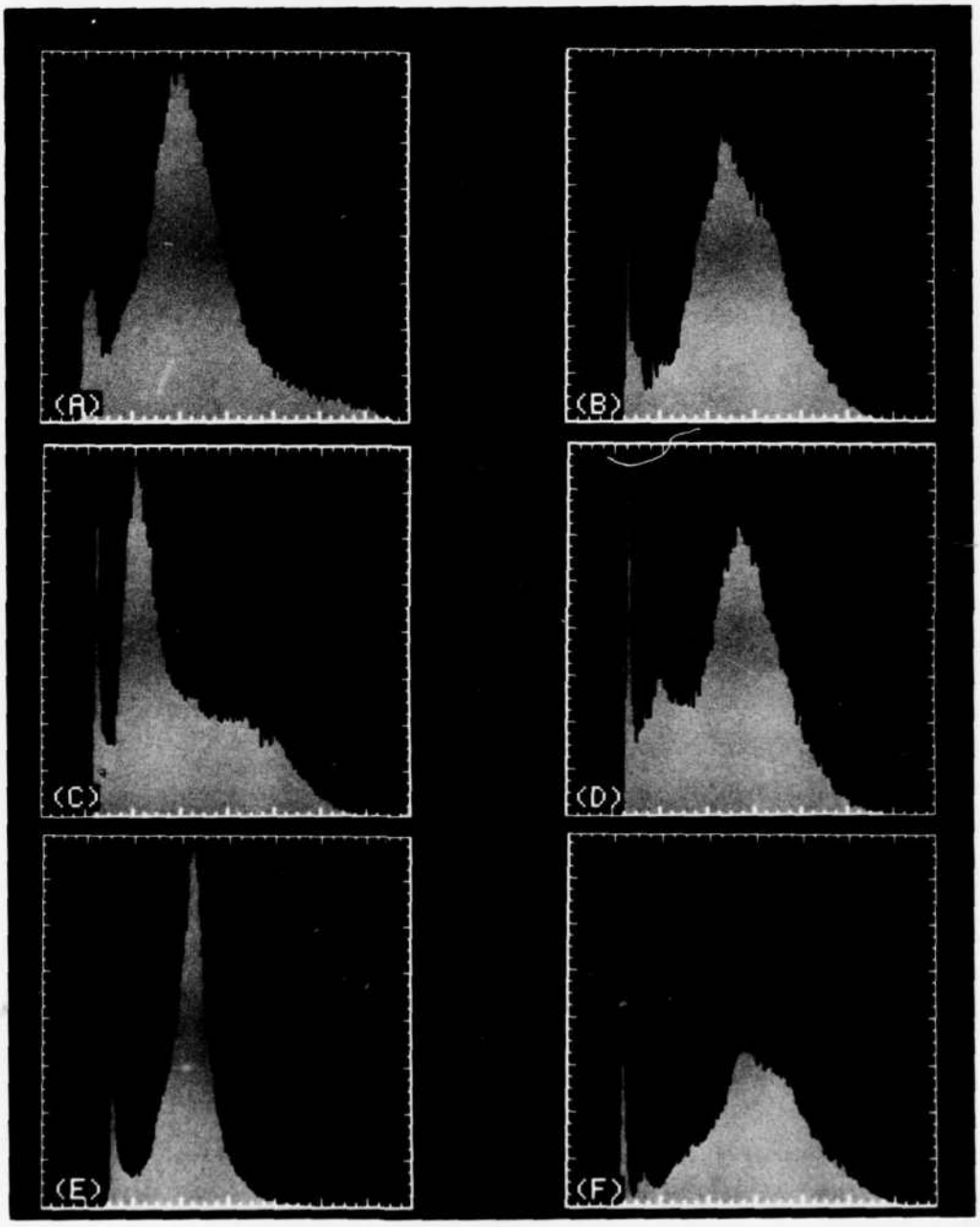

FIGURE 11 - Histograms showing the distribution of intensities in Landsat Images A to F. The sharp peaks at low intensity correspond to water and the broader central peaks correspond to land.

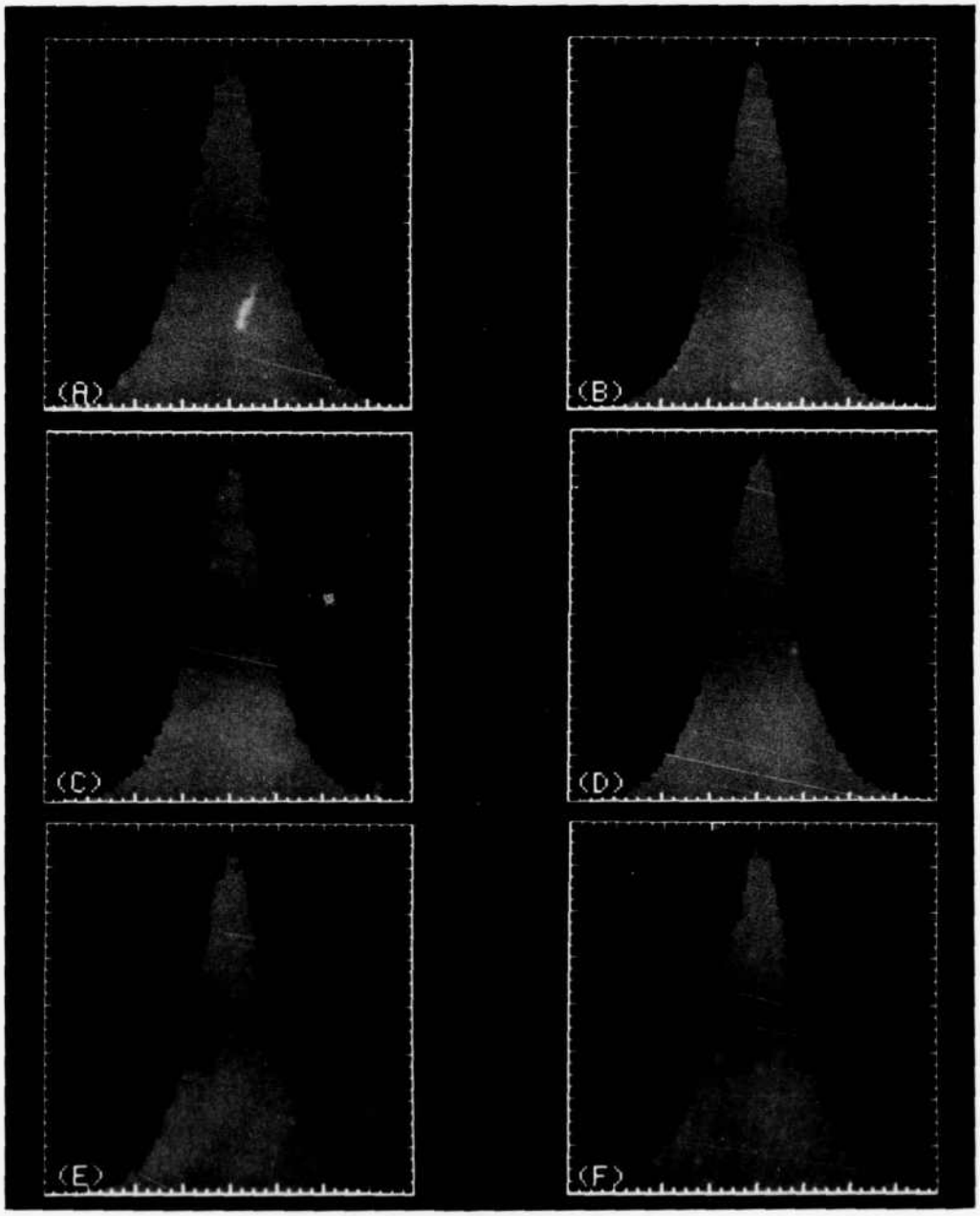

FIGURE 12 - Histograms showing the distribution of intensities in Landsat Images A to F after application of a high-pass filter with a response proportional to the sixth power of the spatial frequency. The filtering has removed the bimodal character evident in Fig. 11 and has produced almost normal intensity distributions.

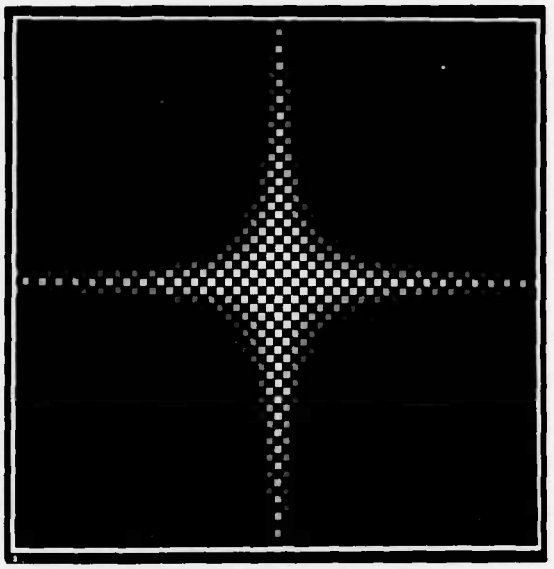

FIGURE 13 - The PSF of a frequency-domain filter with a response proportional to the sixth power of the spatial frequency. Each filter coefficient is displayed as a square element with an intensity proportional to its value. Zero appears with a mid-gray intensity; positive and negative coefficients have higher and lower intensities.

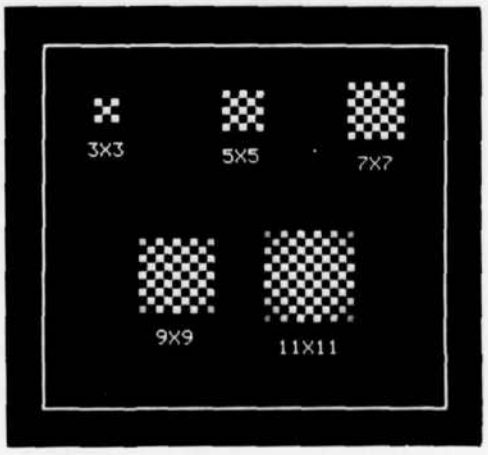

FIGURE 14 - The PSF of Fig. 13 after truncation to form five different small-area approximations

TABLE II

ONE QUADRANT OF THE ω^6 FILTER PSF

1.0000	-0.5912	0.2961	-0.1588	0.0953	-0.0629
-0.5912	0.2817	-0.1114	0.0529	-0.0304	0.0197
0.2961	-0.1114	0.0381	-0.0178	0.0102	-0.0656
-0.1588	0.0529	-0.0178	0.0083	-0.0047	0.0031
0.0953	-0.0304	0.0101	-0.0047	0.0027	-0.0017
-0.0629	0.0197	-0.0066	0.0031	-0.0017	0.0011

the central 64x64-element region of the PSF is displayed, and the value of each filter coefficient is represented by the intensity of a 4x4-element square. The display has been biased so that zero intensity appears gray and positive and negative filter coefficients appear, respectively, lighter and darker than this. We used a nonlinear intensity transformation to improve the visibility of low-intensity positive and negative filter coefficients. The filter is circularly symmetric, so it can be represented by the coefficients within a single quadrant. A listing of the relative values of the coefficients in the lower right quadrant of the PSF is given in Table II. Note that the positive and negative filter coefficients are interleaved.

We generated five filters with PSFs approximating that of the ω^6 one. These were obtained by retaining the filter coefficients within 3x3-, 5x5-, 7x7-, 9x9- and 11x11-element regions of the center of the PSF of the ω^6 filter, and setting to zero all the other coefficients.

The central coefficient of each PSF was then adjusted to obtain a minimum filter response at zero spatial frequency. Figure 14 shows the five resulting truncated PSFs.

Figure 15 shows the result of convolving the five PSFs shown in Fig. 14 with Landsat Image A, along with that obtained by implementing the ω^6 filter with a 2-D FFT. We normalized the display of each filtered image so that full black corresponded to intensity $I_A - 2\sigma$ and full white to intensity $I_A + 6\sigma$. Since the total energy corresponding to the targets is small compared to that of the clutter, the normalization has the effect of displaying the clutter with approximately the same overall contrast in each image. The six filtered images were thresholded at a level of $I_A + 5.5\sigma$, as described in Sect. 4.1, to produce the detected targets shown in Fig. 16.

The clutter remaining after the application of a small-area filter (e.g., one with 3 by 3 or 5 by 5 elements) is more strongly correlated with extended features and edges in the original image than is that remaining after the use of a large-area one (e.g., the 11x11-element or the 2-D FFT filter). For example, the edges of the river are clearly apparent after the application of the 3x3-element filter, whereas these features are barely visible after the application of the 11x11-element and the 2-D FFT filters. As discussed in Sect. 2.1, clutter that is correlated with the edges of extended objects in a scene may be detrimental to certain automatic target-detection and tracking algorithms.

4.3 Comparison of the Spatial Filters

We have graphed in Fig. 17 the number of targets detected in Landsat Image A as a function of the type of high-pass filter that was used. Results are shown for the five convolution filters considered in Sect. 4.2 as well as for the 2-D FFT filter employed in Sect. 4.1. The graphs were obtained as described in Sect. 4.1 for fixed false-alarm

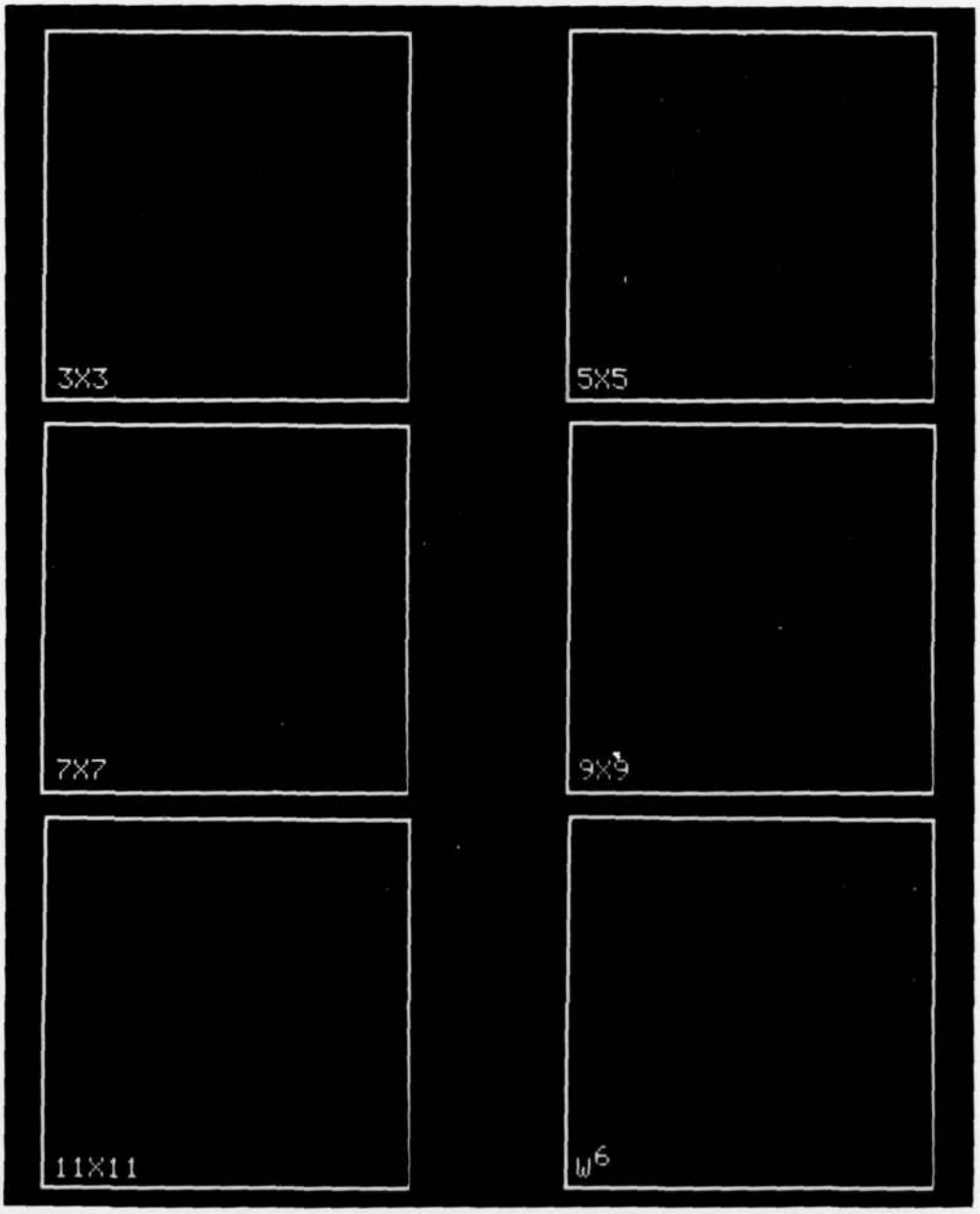

FIGURE 15 - Landsat Image A after high-pass filtering with five different spatial-domain convolution filters and a frequency-domain one with a response proportional to the sixth power of the spatial frequency. Convolution filters with large PSFs (the size is indicated in the lower left of each image) and the frequency-domain filter give better point-target enhancement and rejection of the edges of extended regions of clutter (such as the river).

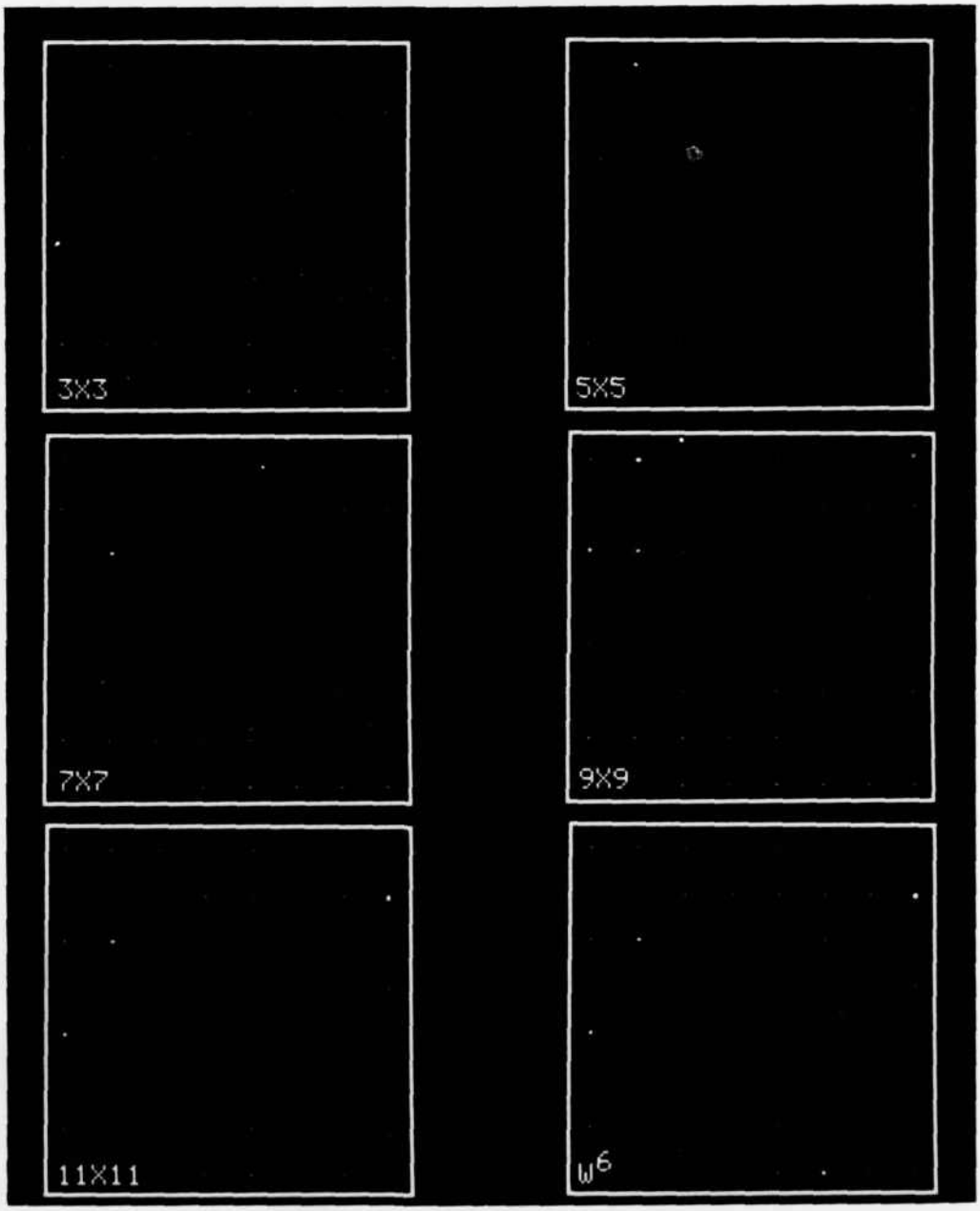

FIGURE 16 - The high-pass filtered images of Fig. 15 after application of a single-intensity threshold at $I_A + 5.5\sigma$ to detect the point targets. Convolution filters with large PSFs (the size is indicated in the lower left of each image), and the frequency-domain filter give better target-detection performance.

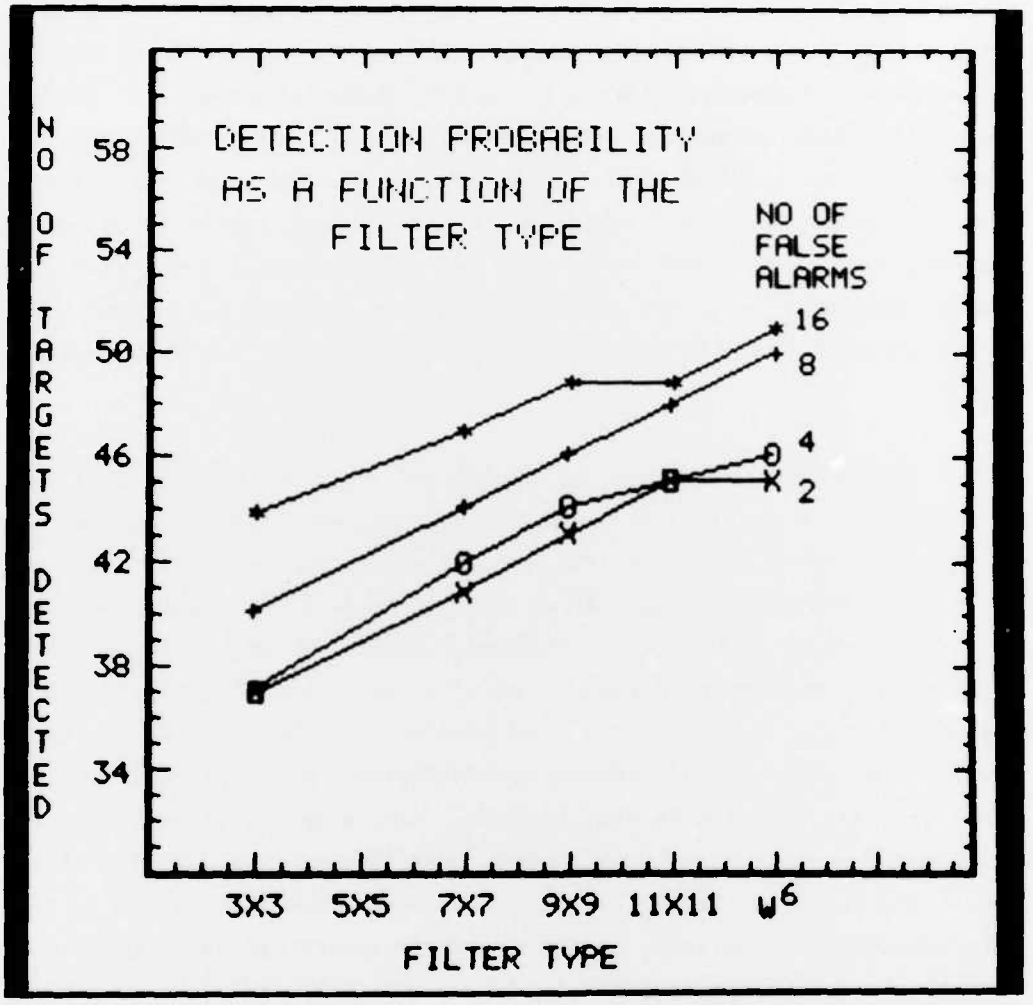

FIGURE 17 - The target-detection performances of the five convolution filters and the frequency-domain filter employed in Fig. 15. We obtained each of the four curves by setting a single-intensity threshold on the filtered images so as to obtain the specified number of false alarms, and then counting how many of the 64 true point targets were detected.

rates of 2, 4, 8 and 16 per image. Figure 17 clearly shows that a filter with a large-area PSF (e.g., 11x11 elements) produces a better target-detection capability than one with a small-area PSF (e.g., 3x3 elements). As noted in Sect. 4.1, in the present case the target-detection probability is a nonlinear function of the number of detected targets, so the observed improvement is a substantial one. For the reason described later in this section, the 5x5-element filter gave poorer results than the 3x3-element one, and we did not plot them in Fig. 17.

As the images of Fig. 15 demonstrate, one reason why a filter with a large PSF is preferable for point-target detection is because it is more effective at attenuating low-frequency clutter that is correlated over relatively large areas of the image. In particular, the edges of extended objects are composed mainly of high spatial frequencies in the direction perpendicular to the edge, but considerable low spatial-frequency content is present in the direction of the edge itself. An edge can be removed by high-pass filtering only if the lowest spatial frequencies that compose it are strongly attenuated, and this requires that the corresponding dimension of the filter PSF be comparable to the effective length of the edge. Intuitively, it is the interleaved positive and negative filter coefficients evident in Fig. 13 that cause the cancellation of an extended edge.

A second reason why a filter with a small PSF is less suitable for point-target detection is because of the difficulty one has in obtaining a frequency response that is circularly symmetric. Both the point targets and the clutter that are typically present in satellite imagery have circularly symmetric spatial-frequency distributions centered on the origin. The high-pass filter required for clutter rejection should therefore have a circularly symmetric frequency response. However, because of the limited number of coefficients, and the rectan-

gular grid on which they are defined, high-pass filters with a frequency response that approximates circular symmetry cannot be obtained by convolving a small PSF.

This is illustrated in Fig. 18, which compares the frequency responses of the five present convolution filters with that of the desired ω^6 filter. We obtained the frequency responses by applying each filter to an image containing a point against a zero background, and then calculating the modulus of its 2-D FFT. The gray level of each display is proportional to the logarithm of the frequency response, with full white representing 0 dB and full black -80 dB. The zero spatial frequency is at the center of each display.

Note the prominent lobe structures and the highly directional nature of the frequency responses of the filters obtained by convolving small PSFs. Only the 11x11-element filter approximates the desired ω^6 response. The presence of lobe structures and other deviations from circular symmetry in the frequency response of a 2-D filter will introduce artificial directional structure into the filtered images. In particular, the asymetry will enhance clutter in particular spatial directions, and the lobe structure will enhance clutter that has specific periodicities.

Examination of the filtered images of Fig. 15 reveals these artifacts. The 5x5-, 7x7- and 9x9-element filters have produced a preferential enhancement (i.e., a reduced attenuation) of clutter oriented in the two diagonal directions relative to that with a vertical or a horizontal orientation. In addition to this directionality, the clutter present in the three images also has a periodic nature. This is caused by the local response maxima and minima that the three filters possess in the mid-frequency range. In comparison, the clutter present in the image of Fig. 15, filtered with the 2-D FFT, shows an insignificant amount of directional or periodic structure and the effects are only slightly evident in the image filtered with the 11x11-

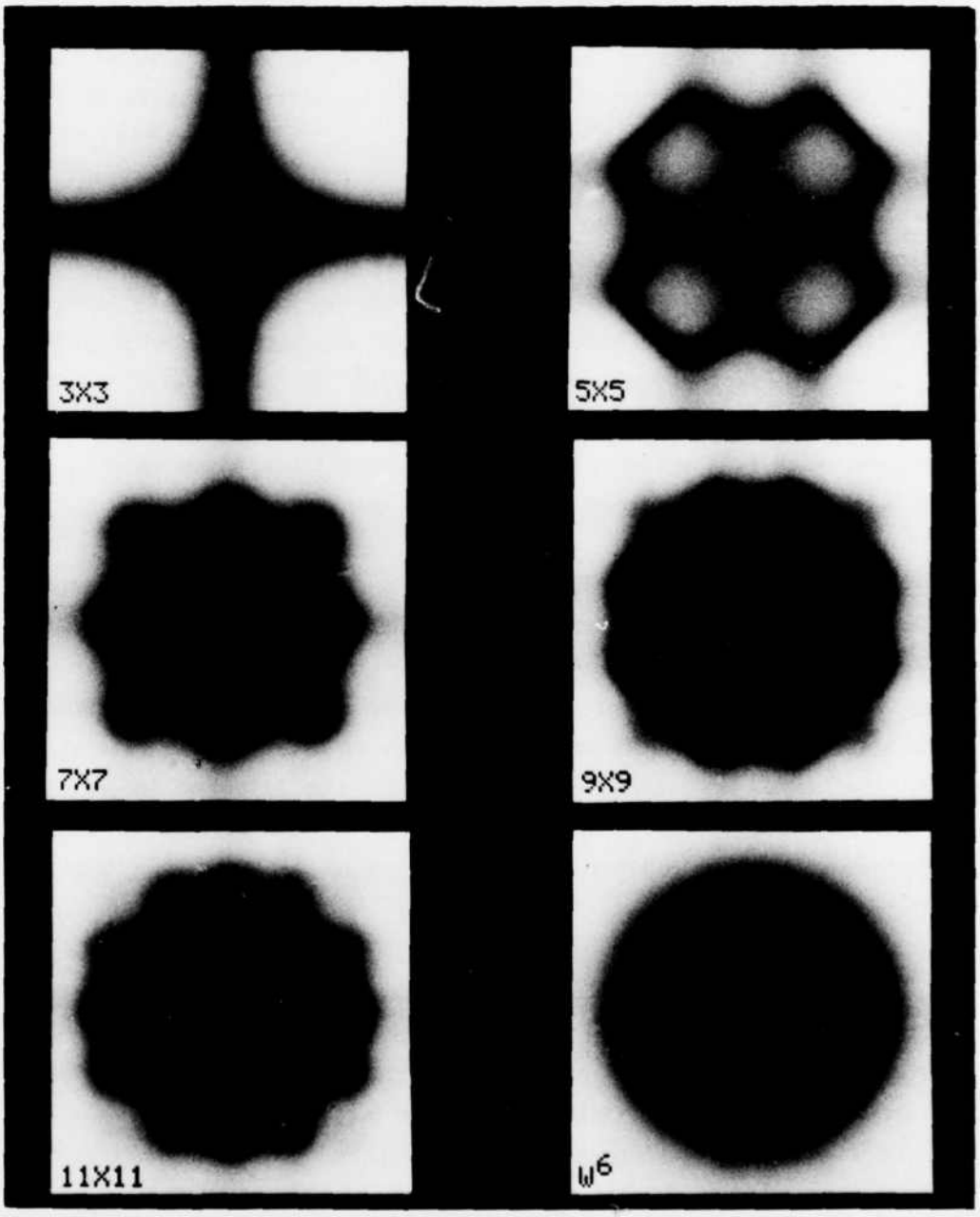

FIGURE 18 - The frequency responses of the five convolution filters and the frequency-domain one employed in Fig. 15. Zero spatial frequency is at the center of each image and the two axes correspond to the horizontal and vertical spatial frequencies. The intensity of the display is proportional to the logarithm of the filter response with full black corresponding to -60 dB. The small area convolution filters deviate significantly from the desired circular symmetry.

element PSF. The strong presence of these artifacts in the image filtered with the 5x5-element PSF may explain why the point-target-detection performance of this filter was significantly poorer than even that of the 3x3-element filter.

5.0 CONCLUSIONS

Spatial filtering can enhance point targets located in a cluttered background in images obtained from a satellite-based mosaic IR detector. We examined by simulation and compared the target-detection performances of a variety of spatial filters implemented by direct convolution and by 2-D FFT filtering.

When a single-intensity threshold is used to detect the targets, it is preferable to use a spatial filter that produces considerably more high-frequency enhancement than a conventional Wiener filter. We found that a filter with a frequency response proportional to the sixth power of the spatial frequency was effective at enhancing the point targets and rejecting the clutter in the present test imagery. For comparison, the corresponding Wiener filter had an approximate frequency response between the square and the cube of the spatial frequency.

Convolution filters with large-area PSFs (e.g., 11x11 elements), and those implemented in the spatial-frequency domain with a 2-D FFT, are more effective than filters with small-area PSFs (e.g., 3x3 elements) at attenuating the edges of extended clutter regions. In addition, filters with small PSFs have spatial-frequency responses that are not circularly symmetric and which can possess lobe or directional features. These properties can introduce undesirable artifacts and can reduce the clutter-rejection effectiveness.

The processing required to detect and track targets from a space-based surveillance system will include temporal and multispectral processing, as well as the spatial filtering of individual image frames considered here. In future, we will examine how temporal and multispectral processing can be incorporated into the overall processing. However, such processing algorithms will be particularly dependent on the characteristics of the imaging system (e.g., signal-to-noise ratio, spatial resolution, frame rate, multispectral response, etc.) and on the imaging scenario (e.g., the characteristics of the target and the background, viewing geometry, satellite jitter, etc.). Realistic imagery obtained with a space-based mosaic IR detector will be needed to optimize the processing required to perform specific target-detection and tracking tasks.

6.0 REFERENCES

1. Janssens, T.J., "Aerospace Vehicle Detection (AVD): Design Trade-Offs", Proc. SPIE, Vol. 197, pp. 58-61, 1979.

2. Janssens, T.J. and Valdes, S.F., "A Sensor Optimization Program", Proc. SPIE, Vol. 253, pp.24-30, 1980.

3. Neel, R., "Scheduling Measurements to be Made by a Step-Stare Mosaic Infrared Sensor", Proc. SPIE, Vol. 253, pp. 31-39, 1980.

4. Pohlman, R.T., "Earth Scene Dynamics as Viewed by a Satellite - Borne Mosaic Sensor", Proc. SPIE, Vol. 197, pp. 35-40, 1979.

5. Webster, D.C., "The Dynamic Behavior of a Fixed Earth Scene as Viewed by a Satellite-Borne Staring Mosaic Sensor", Proc. SPIE, Vol. 124, pp. 17-22, 1977.

6. Winter, E.M., "Causes of Clutter for Earth Background Staring Sensors", Proc. SPIE, Vol. 253, pp. 2-7, 1980.

7. Pollock, D.H., "Clutter Rejection for Infrared Surveillance Sensors", Proc. SPIE, Vol. 292, pp. 180-192, 1981.

8. Murcray, D.G., Murcray, F.H., Kosters, J.J. and Williams, W.J., "Balloon-Borne Measurements of Infrared (IR) Backgrounds", Proc. SPIE, Vol. 253, pp.187-192, 1980.

9. Liang, A.C., "Statistical Modeling of Infrared (IR) Background due to Spacecraft-Induced Line-of-Sight Jitter", Proc. SPIE, Vol. 197, pp. 30-34, 1979.

10. Wald, L.H., Chou, F.M. and Hines, D.C., "Recent Progress in Extraction of Targets out of Clutter", Proc. SPIE, Vol. 253, pp. 40-55, 1980.

11. Otto, R.G., Kemp, D.D., Hilsenrath, M. and Golosman, B.S., "Space Surveillance Signal Processor (S^3P) for Background Suppression and Target Detection with a Staring Mosaic Sensor", Proc. SPIE, Vol. 241, pp. 20-28, 1980.

12. Longmire, M.S., Milton, A.F. and Takken, E.H., "Simulation of Clutter Rejection Signal Processing for Mid-Infrared Surveillance Systems", Proc. SPIE, Vol. 292, pp. 193-203, 1981.

13. Rauch, H.E., Futterman, W.I. and Kemmer, D.B., "Background Suppression and Tracking with a Staring Mosaic Sensor", Proc. SPIE, Vol. 197, pp.19-29, 1979.

14. Boulter, J.F., Corriveau, R., Blanchard, A. and Boudreault, Y., "Space-Based IR Systems Study: Familiarization Phase", DREV R-4275, UNCLASSIFIED

15. Huang, T.S., Schreiber, W.F. and Tretiak, O.J., "Image Processing", Proc. IEEE, Vol. 59, pp.1586-1609, November 1971.

16. Boulter, J.F., "Digital Restoration of Blurred Photographs", DREV R-4107/78, February 1978, UNCLASSIFIED

17. Boulter, J.F., "Target Tracking by Image Subtraction", DREV R-4226/82, January 1982, UNCLASSIFIED

18. Kirvida, L. and Pirich, A.R., "Change Detection Using Infrared (IR) Imagery", Proc. SPIE, Vol. 137, pp. 51-56, 1978.

19. Rauch, H.E. and Firschein, O., "Automatic Track Assembly for Thresholded Infrared Images", Proc. SPIE, Vol. 253, pp. 75-85, 1980.

20. Firschein, O., Rauch, H.E. and Eppler, W.G., "Track Assembly and Background Suppression Using an Array Processor and Neighborhood Coding", Proc. SPIE, Vol. 241, pp. 258-266, 1980.

21. Boulter, J.F., "Interactive Digital Image Restoration and Enhancement", Comp. Graphics and Image Proc., Vol. 9, pp. 301-312, December 1979. Also published as DREV R-4143/79, July 1979, UNCLASSIFIED

22. Mackey, P., Barone, F.R. and Chu, N.A., "Real-Time Nonuniformity Correction for Focal Plane Arrays Using 12-Bit Electronics", Proc. SPIE, Vol. 292, pp. 210-217, 1981.

23. Hsing, T.R., "Correction of Pixel Nonuniformities for Solid-State Imagers", Proc. SPIE, Vol. 292, pp. 218-224, 1981.

24. Boulter, J.F., "Use of Spatial Filtering to Match Wide Dynamic Range Grayscale Imagery to a Lower Resolution Display", DREV R-4074/77, January 1977, UNCLASSIFIED

CRDV R-4287/83 (NON CLASSIFIE)

Bureau - Recherche et Développement, MDN, Canada.
CRDV, C.P. 8800, Courcelette, Qué. G0A 1R0

"Filtrage spatial à rehausser des cibles ponctuelles dans des images obtenues par un système de surveillance embarqué sur satellites"
par J.F. Boulter

Nous avons examiné par simulation l'aptitude du filtrage spatial à rehausser la visibilité des cibles ponctuelles et à réduire l'arrière-plan dans des images obtenues par un système de surveillance, embarqué sur satellites, employant une mosaïque de détecteurs IR. Un système expérimental de traitement numérique d'images fut employé pour traiter interactivement des images obtenues par le satellite Landsat II auxquelles des cibles ponctuelles simulées étaient ajoutées. Premièrement, les filtres qui accentuent les hautes fréquences sont préférables au filtre standard du type Wiener. Ils sont plus efficaces pour détecter les cibles et éliminer l'arrière-plan. Deuxièmement, les filtres convolutionnels utilisant une fonction avec une grande surface (e.g. 11 x 11 éléments ou ceux obtenus en utilisant une transformation de Fourier bidimensionnelle) sont plus efficaces pour éliminer les contours des grands objets de l'arrière-plan (e.g. les nuages, les lacs, etc.) que les filtres avec une petite surface (e.g. 3 x 3 ou 5 x 5 éléments).

CRDV R-4287/83 (NON CLASSIFIE)

Bureau - Recherche et Développement, MDN, Canada.
CRDV, C.P. 8800, Courcelette, Qué. G0A 1R0

"Filtrage spatial à rehausser des cibles ponctuelles dans des images obtenues par un système de surveillance embarqué sur satellites"
par J.F. Boulter

Nous avons examiné par simulation l'aptitude du filtrage spatial à rehausser la visibilité des cibles ponctuelles et à réduire l'arrière-plan dans des images obtenues par un système de surveillance, embarqué sur satellites, employant une mosaïque de détecteurs IR. Un système expérimental de traitement numérique d'images fut employé pour traiter interactivement des images obtenues par le satellite Landsat II auxquelles des cibles ponctuelles simulées étaient ajoutées. Premièrement, les filtres qui accentuent les hautes fréquences sont préférables au filtre standard du type Wiener. Ils sont plus efficaces pour détecter les cibles et éliminer l'arrière-plan. Deuxièmement, les filtres convolutionnels utilisant une fonction avec une grande surface (e.g. 11 x 11 éléments ou ceux obtenus en utilisant une transformation de Fourier bidimensionnelle) sont plus efficaces pour éliminer les contours des grands objets de l'arrière-plan (e.g. les nuages, les lacs, etc.) que les filtres avec une petite surface (e.g. 3 x 3 ou 5 x 5 éléments).

CRDV R-4287/83 (NON CLASSIFIE)

Bureau - Recherche et Développement, MDN, Canada.
CRDV, C.P. 8800, Courcelette, Qué. G0A 1R0

"Filtrage spatial à rehausser des cibles ponctuelles dans des images obtenues par un système de surveillance embarqué sur satellites"
par J.F. Boulter

Nous avons examiné par simulation l'aptitude du filtrage spatial à rehausser la visibilité des cibles ponctuelles et à réduire l'arrière-plan dans des images obtenues par un système de surveillance, embarqué sur satellites, employant une mosaïque de détecteurs IR. Un système expérimental de traitement numérique d'images fut employé pour traiter interactivement des images obtenues par le satellite Landsat II auxquelles des cibles ponctuelles simulées étaient ajoutées. Premièrement, les filtres qui accentuent les hautes fréquences sont préférables au filtre standard du type Wiener. Ils sont plus efficaces pour détecter les cibles et éliminer l'arrière-plan. Deuxièmement, les filtres convolutionnels utilisant une fonction avec une grande surface (e.g. 11 x 11 éléments ou ceux obtenus en utilisant une transformation de Fourier bidimensionnelle) sont plus efficaces pour éliminer les contours des grands objets de l'arrière-plan (e.g. les nuages, les lacs, etc.) que les filtres avec une petite surface (e.g. 3 x 3 ou 5 x 5 éléments).

CRDV R-4287/83 (NON CLASSIFIE)

Bureau - Recherche et Développement, MDN, Canada.
CRDV, C.P. 8800, Courcelette, Qué. G0A 1R0

"Filtrage spatial à rehausser des cibles ponctuelles dans des images obtenues par un système de surveillance embarqué sur satellites"
par J.F. Boulter

Nous avons examiné par simulation l'aptitude du filtrage spatial à rehausser la visibilité des cibles ponctuelles et à réduire l'arrière-plan dans des images obtenues par un système de surveillance, embarqué sur satellites, employant une mosaïque de détecteurs IR. Un système expérimental de traitement numérique d'images fut employé pour traiter interactivement des images obtenues par le satellite Landsat II auxquelles des cibles ponctuelles simulées étaient ajoutées. Premièrement, les filtres qui accentuent les hautes fréquences sont préférables au filtre standard du type Wiener. Ils sont plus efficaces pour détecter les cibles et éliminer l'arrière-plan. Deuxièmement, les filtres convolutionnels utilisant une fonction avec une grande surface (e.g. 11 x 11 éléments ou ceux obtenus en utilisant une transformation de Fourier bidimensionnelle) sont plus efficaces pour éliminer les contours des grands objets de l'arrière-plan (e.g. les nuages, les lacs, etc.) que les filtres avec une petite surface (e.g. 3 x 3 ou 5 x 5 éléments).

DREV R-4287/83 (UNCLASSIFIED)

Research and Development Branch, DND, Canada.
DREV, P.O. Box 8800, Courcelette, Que. G0A 1R0

"Spatial Filtering for Enhancing Point Targets in Images from a Space-Based Mosaic IR Detector"
by J.F. Boulter

We examined by simulation the use of spatial filtering for enhancing the visibility of point targets and reducing the background clutter in imagery obtained with a space-based staring mosaic IR detector array. An experimental digital image-processing system was employed to interactively process Landsat II images containing simulated point targets. First, we obtained improved target detection and clutter rejection by using filters that produced considerably more high-frequency enhancement than the conventional Wiener filter. Second, convolution filters with large-area point-spread functions (e.g., those with 11 by 11 elements or those implemented with a 2-dimensional FFT algorithm) were more effective at attenuating the edges of extended regions of clutter (e.g., those corresponding to clouds, bodies of water, etc.) than were those with small areas (e.g., 3 by 3 or 5 by 5 elements).

DREV R-4287/83 (UNCLASSIFIED)

Research and Development Branch, DND, Canada.
DREV, P.O. Box 8800, Courcelette, Que. G0A 1R0

"Spatial Filtering for Enhancing Point Targets in Images from a Space-Based Mosaic IR Detector"
by J.F. Boulter

We examined by simulation the use of spatial filtering for enhancing the visibility of point targets and reducing the background clutter in imagery obtained with a space-based staring mosaic IR detector array. An experimental digital image-processing system was employed to interactively process Landsat II images containing simulated point targets. First, we obtained improved target detection and clutter rejection by using filters that produced considerably more high-frequency enhancement than the conventional Wiener filter. Second, convolution filters with large-area point-spread functions (e.g., those with 11 by 11 elements or those implemented with a 2-dimensional FFT algorithm) were more effective at attenuating the edges of extended regions of clutter (e.g., those corresponding to clouds, bodies of water, etc.) than were those with small areas (e.g., 3 by 3 or 5 by 5 elements).

DREV R-4287/83 (UNCLASSIFIED)

Research and Development Branch, DND, Canada.
DREV, P.O. Box 8800, Courcelette, Que. G0A 1R0

"Spatial Filtering for Enhancing Point Targets in Images from a Space-Based Mosaic IR Detector"
by J.F. Boulter

We examined by simulation the use of spatial filtering for enhancing the visibility of point targets and reducing the background clutter in imagery obtained with a space-based staring mosaic IR detector array. An experimental digital image-processing system was employed to interactively process Landsat II images containing simulated point targets. First, we obtained improved target detection and clutter rejection by using filters that produced considerably more high-frequency enhancement than the conventional Wiener filter. Second, convolution filters with large-area point-spread functions (e.g., those with 11 by 11 elements or those implemented with a 2-dimensional FFT algorithm) were more effective at attenuating the edges of extended regions of clutter (e.g., those corresponding to clouds, bodies of water, etc.) than were those with small areas (e.g., 3 by 3 or 5 by 5 elements).

DREV R-4287/83 (UNCLASSIFIED)

Research and Development Branch, DND, Canada.
DREV, P.O. Box 8800, Courcelette, Que. G0A 1R0

"Spatial Filtering for Enhancing Point Targets in Images from a Space-Based Mosaic IR Detector"
by J.F. Boulter

We examined by simulation the use of spatial filtering for enhancing the visibility of point targets and reducing the background clutter in imagery obtained with a space-based staring mosaic IR detector array. An experimental digital image-processing system was employed to interactively process Landsat II images containing simulated point targets. First, we obtained improved target detection and clutter rejection by using filters that produced considerably more high-frequency enhancement than the conventional Wiener filter. Second, convolution filters with large-area point-spread functions (e.g., those with 11 by 11 elements or those implemented with a 2-dimensional FFT algorithm) were more effective at attenuating the edges of extended regions of clutter (e.g., those corresponding to clouds, bodies of water, etc.) than were those with small areas (e.g., 3 by 3 or 5 by 5 elements).

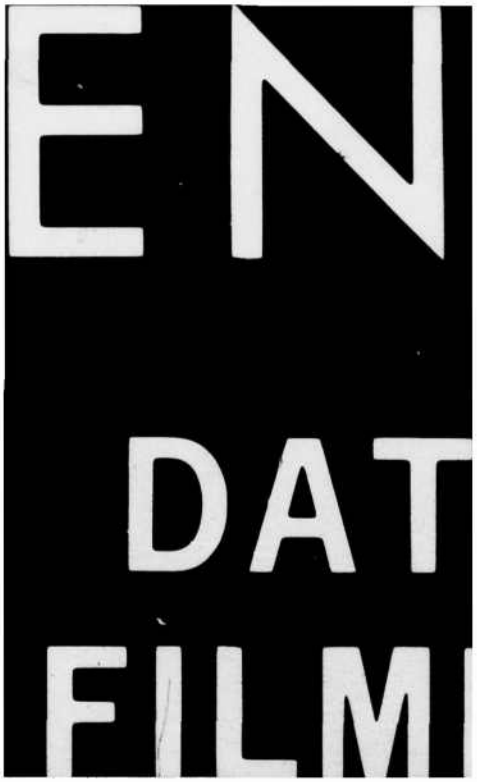
EN
DAT
FILM

We have graphed in Fig. 17 the number of targets detected in Landsat Image A as a function of the type of high-pass filter that was used. Results are shown for the five convolution filters considered in Sect. 4.2 as well as for the 2-D FFT filter employed in Sect. 4.1. The graphs were obtained as described in Sect. 4.1 for fixed false-alarm

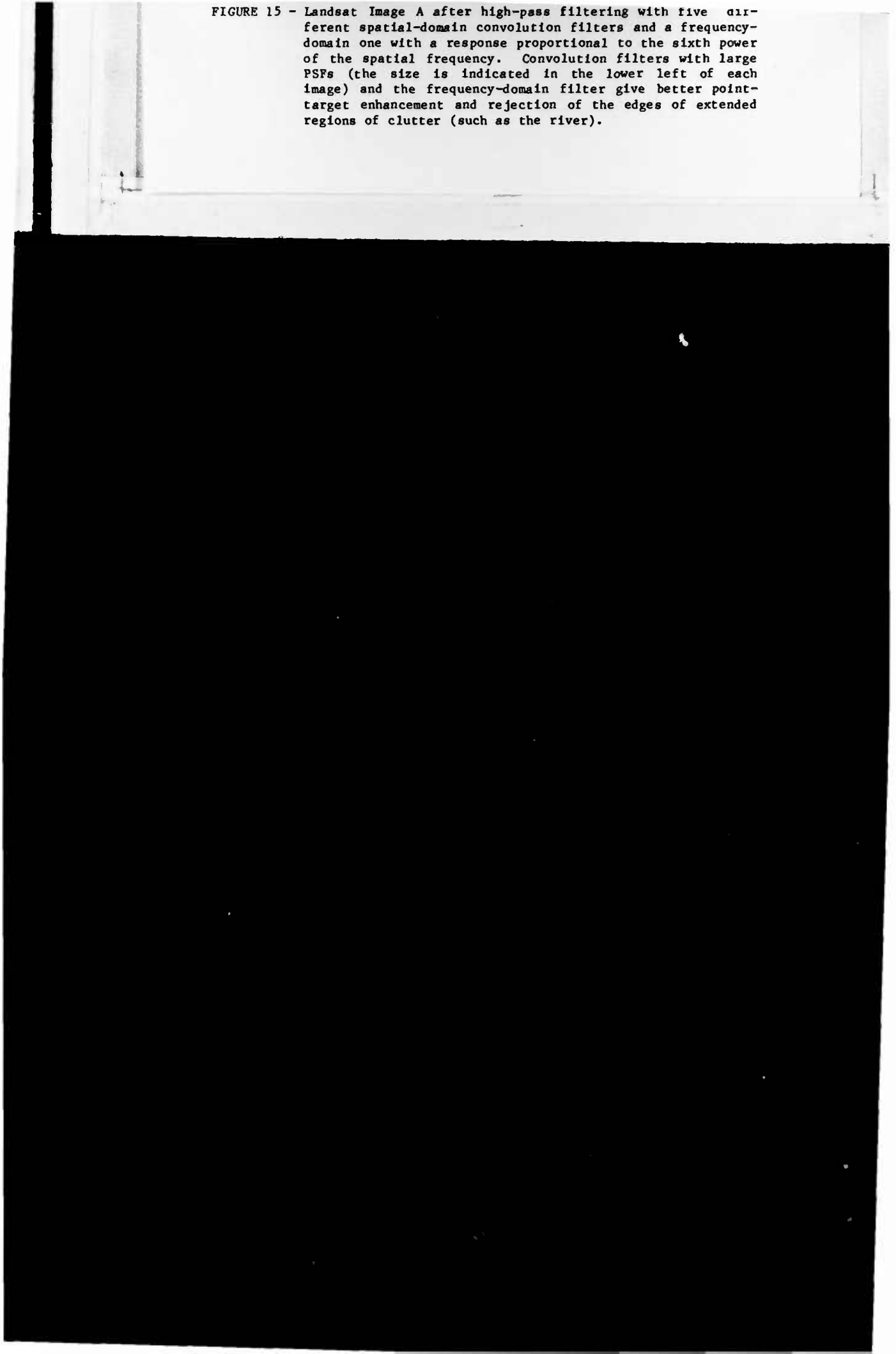

FIGURE 15 - Landsat Image A after high-pass filtering with five different spatial-domain convolution filters and a frequency-domain one with a response proportional to the sixth power of the spatial frequency. Convolution filters with large PSFs (the size is indicated in the lower left of each image) and the frequency-domain filter give better point-target enhancement and rejection of the edges of extended regions of clutter (such as the river).

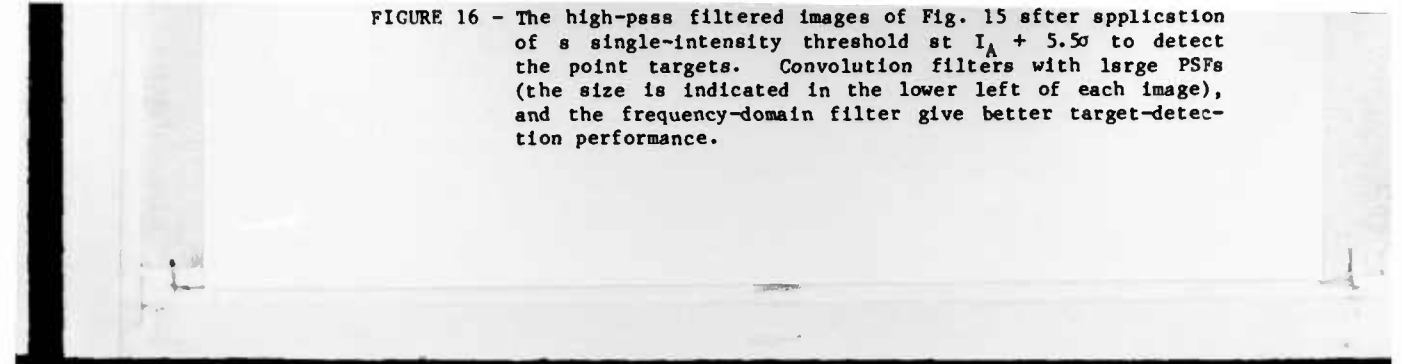

FIGURE 16 - The high-pass filtered images of Fig. 15 after application of a single-intensity threshold at $I_A + 5.5\sigma$ to detect the point targets. Convolution filters with large PSFs (the size is indicated in the lower left of each image), and the frequency-domain filter give better target-detection performance.

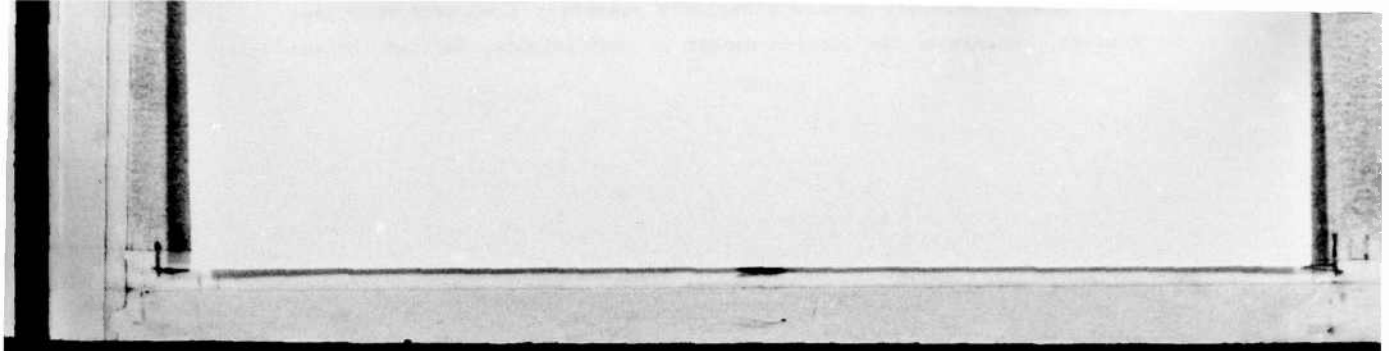

Vol. 241, pp. 20-28, 1980.

12. Longmire, M.S., Milton, A.F. and Takken, E.H., "Simulation of Clutter Rejection Signal Processing for Mid-Infrared Surveillance Systems", Proc. SPIE, Vol. 292, pp. 193-203, 1981.

13. Rauch, H.E., Futterman, W.I. and Kemmer, D.B., "Background Suppression and Tracking with a Staring Mosaic Sensor", Proc. SPIE, Vol. 197, pp.19-29, 1979.

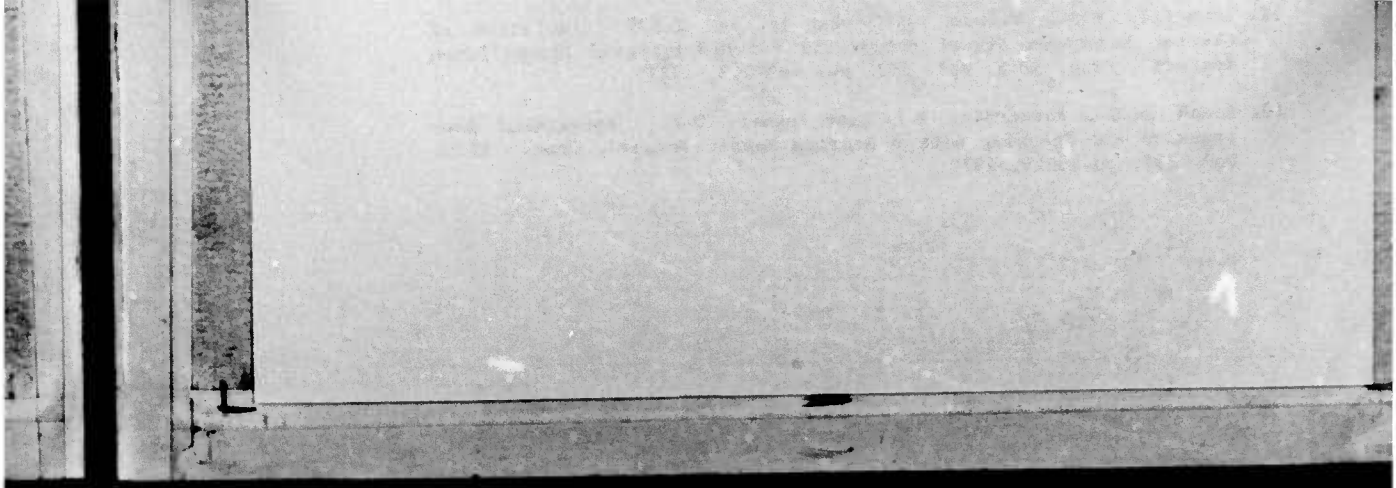

[redacted]


DTI